Linewidth-reduced DBR Laser for Raman Sideband Cooling

Pooja Malik

Masterarbeit in Physik
angefertigt im Institut für Angewandte Physik

vorgelegt der
Mathematisch-Naturwissenschaftlichen Fakultät
der
Rheinischen Friedrich-Wilhelms-Universität
Bonn

May 2020

I hereby declare that this thesis was formulated by myself and that no sources or tools other than those cited were used.

Bonn, 05.05.2020 .....
Date

.....
Signature

1. Gutachter: Prof. Dr. Dieter Meschede
2. Gutachter: Prof. Dr. Simon Stellmer

Contents

1 Introduction **3**

2 Laser Linewidth Reduction via Optical Feedback **5**
2.1 DBR Laser . . . 5
2.1.1 Wavelength Tunability . . . 6
2.2 Theory of Optical Feedback : Modified Rate Equations . . . 7
2.2.1 Steady-State Behaviour . . . 8
2.2.2 Laser Linewidth . . . 9
2.2.3 Numerical Solution to Modified Rate Equations . . . 9
2.3 Regimes of Linewidth Reduction in Distributed Feedback Laser . . . 11
2.3.1 Experimental Setup . . . 12

3 Linewidth Measurement **15**
3.1 Delayed Self Heterodyne Measurement . . . 15
3.2 Experimental Setup . . . 17
3.2.1 Frequency Offset Lock . . . 19
3.3 Linewidth Analysis of the DBR Laser . . . 19
3.3.1 Phase Noise in Lasers . . . 21
3.4 Simulation-based Fitting Routine . . . 22
3.4.1 Generating Discrete-time Signal . . . 24
3.4.2 Generating white, $1/f$ and $1/f^2$ Frequency Noise Sources . . . 24
3.4.3 Welch Method . . . 24
3.4.4 Nelder-Mead Simplex Search . . . 26
3.5 Lorentzian Linewidth Estimation : PSD of Phase Noise . . . 29
3.6 Noise Coefficients . . . 29
3.6.1 Estimation of Quadratic Scaling Factors . . . 31
3.7 Pure Lineshape . . . 31
3.8 Conclusion . . . 34

4 Carrier-free Raman Sideband Cooling **35**
4.1 Raman Laser Setup . . . 35
4.2 Raman Sideband Cooling . . . 39
4.2.1 Experimental Setup . . . 39
4.2.2 Motional State Coupling . . . 40
4.2.3 Cooling Scheme . . . 40
4.3 Raman Spectroscopy and Cooling . . . 41
4.3.1 Experimental Sequence for Raman Spectroscopy . . . 41
4.4 Conclusion . . . 45

5 Conclusion 47

Acknowledgements

आचार्यात्पादमादत्ते पादं शिष्यः स्वमेधया।
कालेन पादमादत्ते पादं सब्रह्मचारिभिः।।

Translation of the Sanskrit śloka written above:"The successful completion of a task depends on four factors; one's hard work, teachers, colleagues and luck/circumstances "

First of all, I would like to extend my gratitude to Prof. Dr. Meschede for offering me a thesis project in his research group and Prof. Dr. Simon Stellmer for being my second referee.

I would like to thank Dr. Deepak Pandey, Eduardo Uruñuela, and Dr. Hannes Pfeifer. It is under their constant guidance this thesis took shape. Special thank you to Dr. Hannes Pfeifer for also writing the simulation-based fitting routine.

A big thank you to Dr. Wolfgang Alt who was always willing to discuss problems and provide suggestions at every step of the thesis.

I would also like to thank Maximilian Ammenwerth, Lukas Ahlheit and Madhavakkannan S. for many stimulating scientific and not-so-scientific discussions. Sincere thanks to Richard Winkelmann for always lending me a helping hand with the electronics in the lab.

I am grateful to all the group members for always being so willing to share their knowledge and experience in the group meetings.

Last but not the least, I thank my family and friends for their unconditional love and support throughout my time in Germany.

CHAPTER 1

Introduction

In our group, we perform Cavity Quantum Electrodynamics (CQED) experiments with single, neutral ^{87}Rb atoms, trapped at the centre of a Fiber-based Fabry Pérot cavity with sub-wavelength precision [1], with the current focus on the aspects of storage of short light-pulses in such platforms [1–3]. The atom is confined in x, y plane using a pair of counter-propagating, red-detuned dipole trap beams and the vertical confinement in the z-axis is provided by an intra-cavity blue detuned optical lattice (lock laser) at 770 nm. The experiment demands extraordinary level of control over the internal and the external degrees of freedom of the trapped atom. In order to prepare these trapped atoms with high probability in their motional ground state, we use carrier-free Raman sideband cooling [4, 5] together with dipole-trap-assisted degenerate Raman sideband cooling (dRSC) as a pre-cooling mechanism [6, 7]. The efficiency of the cooling schemes is quantified by the trapping lifetime of the atom inside the cavity amidst all the heating mechanisms [8, 9]. Longer lifetime increases the rate of recycling of the same atom inside the cavity for multiple measurement attempts. In the past, we could recycle an atom for 10000 photon storage attempts. Another important aspect of single atom experiments is to achieve a high duty cycle of the experiment to attain reasonable statistical error on the experimental data, accomplished by stable laser systems and robust locking schemes.

In the past, we already had a working Raman sideband cooling setup using an interference filter (IF) laser [10] phase locked to the lock laser at ~6.8 GHz. The IF laser used a 780 nm laser diode, tuned to the edge of its gain profile to emit at 770 nm. This laser was not stable, as it would become multi-mode every three hours and fall out of lock. This limited strongly the duty cycle of the experiment. During the first part of the project, I investigated the possibility of a widely tunable DBR laser as a replacement of the IF laser. For Raman sideband cooling this required phase locking the DBR laser at 6.8 GHz frequency difference to the lock laser. With 89 % power in the carrier and locking bandwidth of >2 MHz the phase lock was implemented. Unfortunately, we observed no Raman cooling with the new lock. The failure of the Raman cooling was attributed to the 736.8 kHz Lorentzian linewidth of the DBR laser. This linewidth component arises from random phase fluctuations of the laser (pure white frequency noise) [11, 12]. The corresponding single-sided frequency noise power spectral density (PSD) $S_\nu(f)$ for this noise is flat in frequency, hence uncompensated by the phase lock at higher frequencies and limiting the coherence of an optical phase lock. However, one can reduce the intrinsic linewidth of the laser by means of optical feedback [13–17].

In this thesis, I present how the Lorentzian linewidth of the DBR laser was reduced by implementing an external optical feedback path [18]. Chapter 2 deals with the theoretical framework of effects of the external optical feedback on semiconductor laser and regimes of feedback in distributed feedback lasers [19]. To measure and quantify the linewidth of the DBR laser subject to controlled optical feedback, a

delayed-self heterodyne [20] measurement was setup and is described in Chapter 3. DBR lasers are affected not only by white frequency noise but also low-frequency flicker and random walk noise [21–23]. These noise components restrict the analysis of the DSH spectrum analytically, hence a simulation based fitting routine based on [24] is used. A comprehensive analysis of the Lorentzian linewidth is presented. An estimate on the linewidth arising from the flicker and random-walk frequency noise is also presented in this thesis. With this improvement to the DBR laser, I present in Chapter 4, the implementation of carrier-free Raman sideband cooling [2, 4] in the main experiment.

CHAPTER 2

Laser Linewidth Reduction via Optical Feedback

Distributed Bragg reflector (DBR) laser diodes provide wavelength dependent losses inside the laser cavity [25] which makes them superior to the conventional Fabry Pérot laser diodes. However, due to the small resonator length the Schawlow–Townes–Henry (STH) linewidth [11, 12] of these laser is of the order of a few MHz [26]. This linewidth component arises from random phase fluctuations (white frequency noise) of the laser induced by spontaneous emissions [12]. The corresponding single-sided frequency noise power spectral density (PSD) $S_\nu(f)$ for this noise is flat in frequency, limiting the coherence of an optical phase lock. However, one can reduce the intrinsic linewidth of the laser by means of optical feedback [13–17].

The operation characteristics of a bare laser are strongly affected when a portion of the laser's emitted light is coupled back into the laser cavity after being reflected from an external surface like a mirror or a grating. In most of the cases, these reflections are undesirable and often Faraday isolators are used to block any unwanted reflections. However, controlled optical feedback can be used to enhance the longitudinal mode selection, which yields a narrowed emission spectrum width [16, 27]. The effect of an external feedback on the laser depends strongly on the feedback power, length of the external feedback path, and the phase of the feedback light. Tkach and Chraplyvy categorised the behaviour of distributed feedback lasers under optical feedback in five regimes. These regions were mapped as a function of the feedback power ratio p (ratio of the feedback power to emitted power) and length of the external feedback path d [19].

In this chapter, I briefly discuss the working principle of a DBR laser. Then, I present a theoretical description of optical feedback which modifies the rate equations of a bare laser, and subsequently the effect it has on frequency, gain and the linewidth of the bare laser. Followed by a short overview of the paper by Tkach and Chraplyvy, in which they experimentally verified the different effects of optical feedback on a distributed feedback laser (DFB) at wavelength of 1.5 µm. Finally, I describe the optical feedback configuration used to reduce the linewidth of our 770 nm DBR laser.

2.1 DBR Laser

Unlike most of the lasers where the gain medium is placed between a pair of reflecting surfaces providing the optical feedback, a DBR laser uses a Bragg-type diffraction grating to deflect an optical beam [28]. This Bragg-type diffraction grating is arranged outside the active region at the ends of the laser cavity (Fig. 2.1) and act then as a wavelength selective reflector. The corrugation of alternating refractive index provides 180^o reflection at certain specific wavelengths, depending on the grating spacing λ_l. DBR lasers are single-frequency lasers with diffraction-limited output and have frequency tunability of several GHz

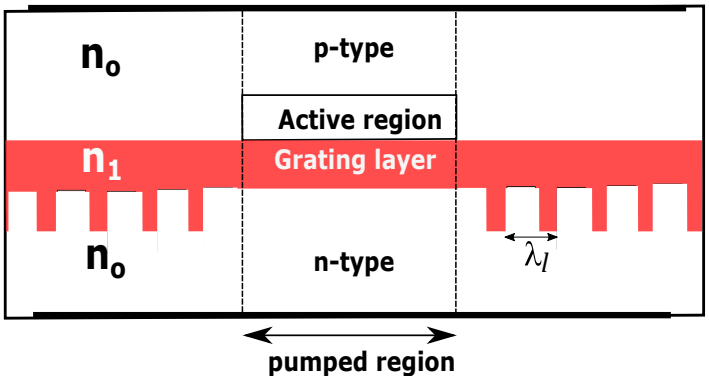

Figure 2.1: Schematic of longitudinal sections in a DBR diode. The periodic index perturbation is induced by different refractive indices n_1 and n_o on opposite sides of the grating. The period of the grating structure is marked by λ_l [28].

without mode-jumps.

2.1.1 Wavelength Tunability

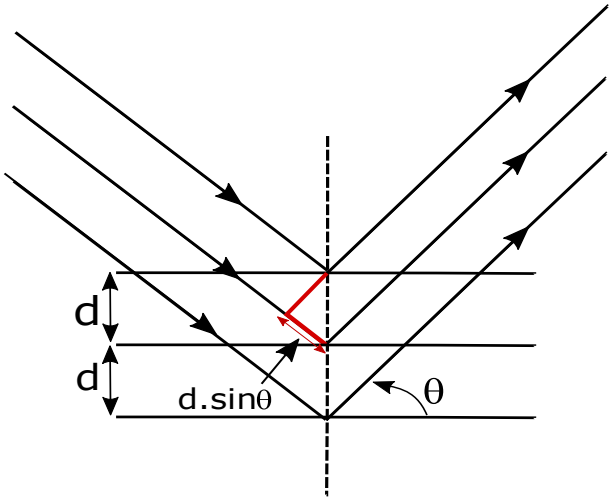

Figure 2.2: Bragg reflection from a periodic structure [29].

The selection of wavelength inside the laser cavity is provided by the Bragg-type grating. As the name suggests, it is based on the principle of Bragg reflection in an atomic crystal. Fig. 2.2 illustrates the reflection of an incident plane wave by a series of reflectors spaced at a distance d. In contrast to the original case of x-ray diffraction where these reflectors are atomic planes of a crystalline lattice, the reflections inside the laser cavity arise from the corrugated grating. As can be seen in Fig. 2.2, for constructive interference, the path lengths for reflections from successive reflectors must be an integer multiple of the wavelengths [29], given by

$$2d \sin\theta = n\lambda, \qquad n = 1, 2, \ldots \tag{2.1}$$

where θ is the angle formed by the incident ray and the reflector and λ is the optical wavelength in

the medium. In the case of 180° reflection by a grating (inside the DBR laser), it is sufficient to have d equal the grating spacing $\lambda_l = \lambda_o/n_g$, where n_g is the effective refractive index in the waveguide for the mode under consideration which depends on refractive index n_1 and n_o. Under these conditions Eq. 2.1 becomes

$$2\lambda_l = n\left(\frac{\lambda_o}{n_g}\right), \qquad n = 1, 2, ... \tag{2.2}$$

Rearranging the above equation gives us the vacuum wavelength of the light that will be emitted by such a grating

$$\lambda_o = 2\lambda_l \frac{n_g}{n}, \qquad n = 1, 2, ... \tag{2.3}$$

From this equation one can see that the grating can support various longitudinal modes depending on the value of 'n' but only one mode will lie within the gain bandwidth of the laser.

The wavelength of the DBR laser can be tuned by changing the effective refractive index n_g. This can be achieved by either altering the temperature of the laser or by changing the injection current in gain section. The change of the refractive index with temperature is the dominant tuning mechanism whereas changes in carrier density due to change in current have a smaller effects on the lasing wavelength.

2.2 Theory of Optical Feedback : Modified Rate Equations

To understand the effect of optical feedback on the laser performance, we need to modify the rate equations of a bare laser. Consider a three-mirror configuration (Fig. 2.3) wherein an external mirror is placed at a distance d from the laser facet. The external mirror and the laser facet form an external cavity which along with the already existing diode cavity makes it a coupled cavity problem. However, multiple reflections in the external cavity can be neglected if the external mirror's reflection coefficient $r_{\text{ext}} \ll 1$ and one can focus on the laser cavity only. The full treatment for $r_{\text{ext}} \not\ll 1$ can be found in [30]. In the plane wave and the slowly varying envelope approximations, the use of the cavity field

$$E_{\text{c}}(z, t) = \text{Re}[E(t)\exp(-i\omega_{\text{o}}t)]\sin(kz) \tag{2.4}$$

in the wave equation leads to [14]

$$\dot{E}(t) = i(\omega_{\text{o}} - \omega_{\text{th}})E(t) + \frac{1}{2}(G - \gamma)(1 - i\beta_{\text{c}})E(t) + \kappa E(t - \tau)\exp(i\phi_{\text{o}}) \tag{2.5}$$

where ω_{th} is the mode frequency of the solitary laser and ω_{o} is the mode frequency in the presence of the feedback. Further, G is the net rate of stimulated emission and γ the cavity-decay rate which accounts for both the facet loss as well as the internal loss. The parameter β_{c} which depends on the carrier-induced refractive change is commonly referred to as the linewidth enhancement factor [12].

The last term in Eq. 2.5 is the consequence of the external optical feedback. The parameters κ and ϕ_{o} (= $\omega_{\text{o}}\tau$, where τ is the external-cavity round-trip time) represent the feedback-coupling rate and the external-cavity phase shift, respectively. During each round trip in the external cavity, the field immediately after reflection inside the laser facing the external cavity is

$$E'(t) = (r_{\text{c}})E(t) + (1 - r_{\text{c}}^2)(r_{\text{ext}})E(t - \tau)\exp(i\omega_{\text{o}}\tau) \tag{2.6}$$

where r_{c} is the reflection coefficient of the diode's facet. Eq. 2.6 shows that during each round trip inside

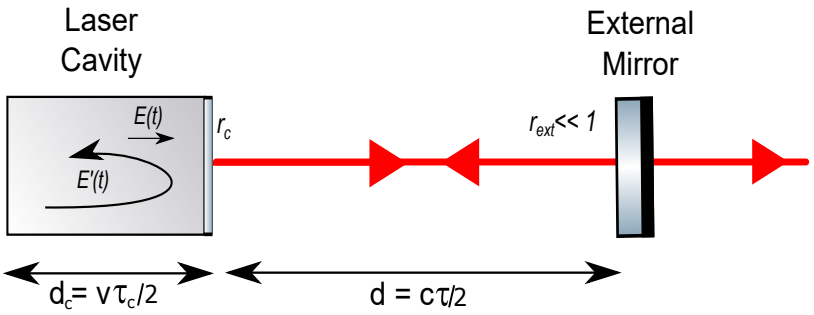

Figure 2.3: The laser cavity along with the external mirror placed at distance d from the laser's facet. E(t) is the laser cavity field whereas E′(t) is the modified laser cavity field immediately after one reflection from the external mirror. r_c and r_{ext} are the reflection coefficient of the laser facet and the external mirror, respectively. τ_c and τ are the round-trip time inside the cavity and in the external feedback path, respectively.

the laser-cavity, a small fraction $(1 - r_c^2)(r_{ext})/(r_c)$ of intra-cavity field re-enters the laser-cavity after some delay and with an additional phase. Let the laser-cavity round-trip time be τ_c, then the coefficient κ can be expressed as

$$\kappa = \frac{(1 - r_c^2) r_{ext}}{r_c \tau_c} \tag{2.7}$$

Using $E = \sqrt{I} e^{-i\phi}$ in Eq. 2.5, we obtain the two coupled rate equations

$$\dot{I}(t) = (G - \gamma) I(t) + R_{sp} + 2\kappa [I(t) I(t - \tau)]^{1/2} \cos[\phi(t) - \phi(t - \tau) + \phi_o] \tag{2.8}$$

$$\dot{\phi}(t) = \frac{\beta_c}{2}(G - \gamma) - (\omega_o - \omega_{th}) - \kappa [\frac{I(t - \tau)}{I(t)}]^{1/2} \sin[\phi(t) - \phi(t - \tau) + \phi_o] \tag{2.9}$$

where in Eq. 2.8, R_{sp} represents the rate at which spontaneously emitted photons are added to the intra-cavity photon population [31]. The effect of external feedback is included via κ and in the case $\kappa = 0$, Eq. 2.8 and Eq. 2.9 reduce to the single-mode rate equations of a solitary laser.

2.2.1 Steady-State Behaviour

The rate equations obtained in Eq. 2.8 and Eq. 2.9 can be solved for steady-state behaviour after assuming $\dot{I} = 0$, $\dot{\phi} = 0$. For simplicity we can neglect R_{sp}, which mostly modifies the threshold sharpness [31]. In the absence of reflection feedback ($\kappa = 0$), the solution is

$$G(\kappa = 0) = \gamma \qquad \omega_o(\kappa = 0) = \omega_{th} \tag{2.10}$$

Let ΔG and $\Delta\omega$ be the change in gain and frequency introduced by external optical feedback, respectively. The solution for ΔG and $\Delta\omega$ in steady state can be expressed as

$$\Delta G = -2\kappa \cos(\omega_o \tau) \tag{2.11}$$

$$\Delta\omega = \omega_o - \omega_{th} = \kappa [\sin(\omega_o \tau) + \beta_c \cos(\omega_o \tau)] \tag{2.12}$$

For given values of κ (strength of the feedback) and τ (external-cavity round-trip time), Eq. 2.11 and

Eq. 2.12 describe the steady-state characteristics of a solitary laser under optical feedback. Solution to these equations can be obtained by numerically solving Eq. 2.12. The values obtained for frequency change $\Delta\omega$ can then be used to obtain the gain change ΔG.

2.2.2 Laser Linewidth

Before describing the numerical solution for the steady state gain and oscillation frequency due to feedback, let us discuss how optical feedback changes the Lorentzian linewidth of the laser. The Lorentzian linewidth of the laser arises from random phase fluctuations induced by spontaneous emissions [11, 12]. Depending on the relative phase of the externally reflected light, the linewidth of a single longitudinal mode, is narrowed or broadened considerably [15]. The problem can be analyzed theoretically using Eq. 2.8 and Eq. 2.9 after supplementing them with appropriate Langevin noise sources [32]. If the external delay time τ is less than the coherence time of the laser field, the effect of the optical feedback on the linewidth of the bare laser can be expressed as [15]

$$\Delta f \approx \frac{\Delta f_o}{\left[1 + C\cos\left(\omega_o\tau + \tan^{-1}(\beta_c)\right)\right]^2} \tag{2.13}$$

where Δf_o is the bare-laser linewidth given by Schawlow-Townes-Henry formula [33] and $C = \kappa\tau(1+\beta_c^2)^{1/2}$ is the feedback parameter. The equation above suggests that for $\omega_o\tau + \tan^{-1}(\beta_c) = 2m\pi$, the linewidth of the laser can be reduced by a factor $(1 + C)^2$.

2.2.3 Numerical Solution to Modified Rate Equations

To understand how optical feedback alters the frequency, gain and the Lorentzian linewidth of a bare laser, Eq. 2.12 is numerically solved for two cases, when the feedback parameter $C < 1$ (low feedback) and when $C > 1$ (high feedback). Typically, semiconductor lasers have $\beta_c \sim 6$ [19]. The numerical solution obtained for change in frequency $\Delta\omega$, gain ΔG and linewidth $\log\left(\frac{\Delta f}{\Delta f_o}\right)$ are plotted as a function of feedback phase $\omega_{th}\tau$ in Fig. 2.4.

Low Feedback $C < 1$

As the feedback phase $\omega_{th}\tau$ is changed from zero to 2π, in case of low feedback ($C < 1$), for each feedback phase, there is only one solution for frequency implying that the laser oscillates only in one mode. The gain follows a similar behaviour. The linewidth of the laser can either be narrowed or broadened depending on the feedback phase. This range of optical feedback is not useful because the linewidth narrowing depends on the feedback phase which is very hard to control in an experiment.

High Feedback $C > 1$

For higher feedback ($C > 1$), there are multiple steady state solutions for some feedback phase and the laser could jump from one mode to the other. For example, at feedback phase $\pi/2$, the laser frequency could either increase (B), stay almost the same (C) or decrease (A) as marked in Fig. 2.4. The frequency difference between these modes is approximately given by τ^{-1}. These multiple solutions are called *external-cavity modes* (XCM), which appear in the vicinity of the *laser-cavity mode* (LCM), the dominant longitudinal mode of the solitary laser. The amplitude and number of XCM depend upon the distance to the external reflector d and the feedback strength. For feedback phase $\pi/2$, gain difference between

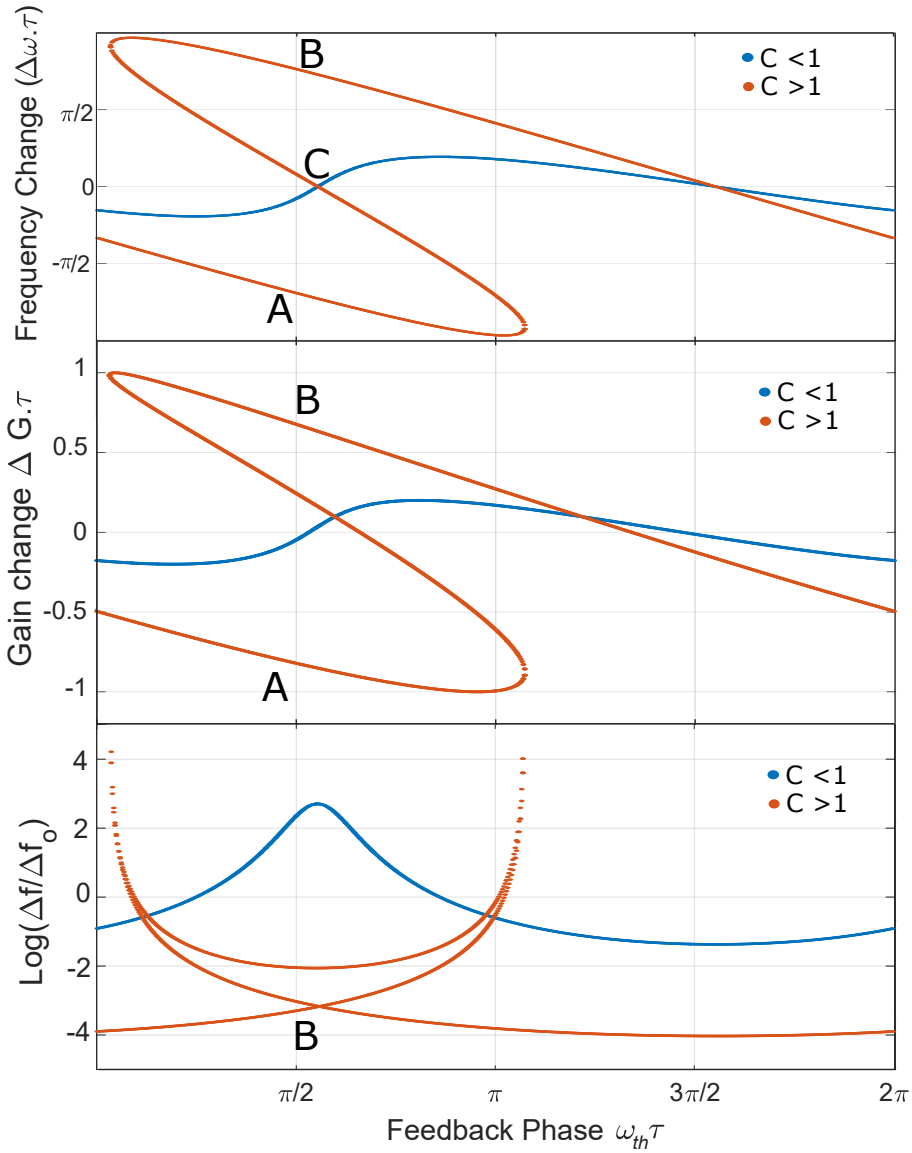

Figure 2.4: Numerical solution to frequency, gain and linewidth change under low ($C < 1$) and high ($C > 1$) optical feedback. At low optical feedback, there is only one solution to frequency and gain, and the laser line is either narrowed or broadened, depending on the phase. For high optical feedback, there are multiple solutions which leads to various effects observed at the higher feedback levels.

different oscillation frequency is significantly higher. The laser preferentially oscillates in the mode with highest gain. The linewidth of the laser in the vicinity of the mode hops can vary significantly by a small change in the feedback phase $\omega_{th}\tau$ in contrast to the low feedback regime.

This complicated operational behaviour of the laser under high optical feedback was experimentally verified and summarised by Tkach and Chraplyvy [19] for a DFB laser at 1.5 µm. In the next section I briefly discuss their findings.

2.3 Regimes of Linewidth Reduction in Distributed Feedback Laser

As shown in [19], the effect of optical feedback can be classified in five regimes (Fig. 2.5):

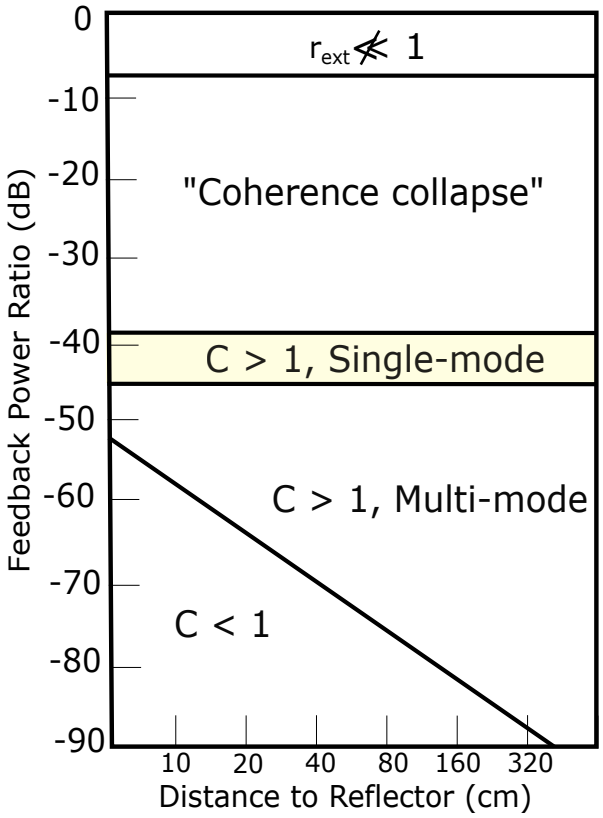

Figure 2.5: Regimes of Optical Feedback Effects in DFB/DBR Laser [19].

Regime 1: This region corresponds to low optical feedback ($C < 1$) where broadening or narrowing of the laser linewidth depends on the distance to the reflector or the phase of the feedback signal.

Regime 2: This region corresponds to $C > 1$ solution where changes in the phase of the feedback leads to mode hopping of the laser between the external-cavity modes (XCM). These solutions are marked by A and B in Fig. 2.4. These modes do not exist simultaneously, the laser hops back and forth between them at a rate which depends on the feedback strength. The linewidth of the laser is broadened for the out of phase feedback and narrowed otherwise.

Regime 3: As the feedback, and the mode spacing is increased (see Eq. 2.12), the dwell time at each mode increases and by increasing the feedback power further the hoping ceases altogether. This stability

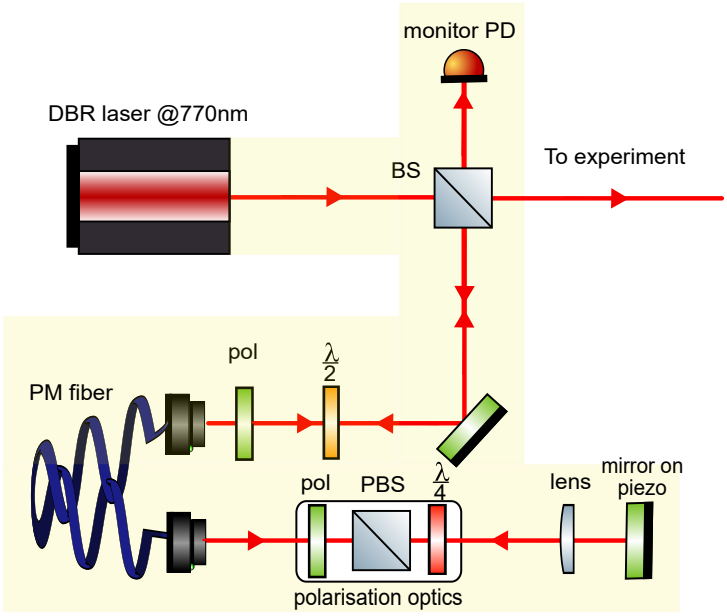

Figure 2.6: Highlighted in yellow is the 2 m long external optical feedback path which couples emitted laser light back into the diode. Four percent of the emitted light reflected at BS is coupled into a PM fiber. From the fiber output, the laser light traverses through polarization optics, is reflected back from a piezo mounted mirror and is finally coupled back to the same fiber and fed back into the diode. The polarisation optics consists of quarter waveplate, PBS and a polariser which regulates the power of the optical feedback. The design of the experimental setup is based on [18].

can be explained by the high gain difference between the XCMs as shown in Fig. 2.4 for the numerical simulation of change in gain ΔG. The laser oscillates in the mode marked by 'B' in Fig. 2.4 because the gain for the corresponding mode is large as compared to other oscillation frequencies. Transition to this regime is relatively independent of the distance to the reflector (d) since the change in gain ΔG introduced by optical feedback (Eq. 2.11) does not depend on the d. The laser linewidth in this regime is reduced, independent of the feedback phase Fig. 2.4. This useful operational behavior is limited to a narrow region ($\approx$−39 dB to −45 dB) of feedback power ratio.

Regime 4: Above 6 dB, relaxation oscillation sidebands appear on the emission line and on increasing the feedback further these sidebands grow and broaden leading to "coherence collapse" [34]. The linewidth of the laser is broadened upto 100 GHz.

Regime 5: In this high feedback regime, the laser cavity is a short active section and the external feedback path becomes the dominant cavity. With a wavelength selective element in the feedback path, the laser operates on a single longitudinal mode with a narrow linewidth for all feedback phases.

The narrow feedback range of Regime 3 could be used for achieving stable, narrow-linewidth operation of a DBR laser. In the next section, I discuss how we setup such an external optical feedback path for our 770 nm DBR laser.

2.3.1 Experimental Setup

To reduce the linewidth of the 770 nm DBR laser, an external optical feedback path [18] is set up (Fig. 2.6) (highlighted in yellow). Four percent of the emitted light reflected at the 90:10 beam splitter (BS) is

coupled into a 1 m long polarisation maintaining (PM) fiber. The polarisation of the input light is linear and oriented along one of the axes of the PM fiber using a set of polariser and half wave plate. From the fiber output, the laser light traverses through polarization optics and is focused on a mirror mounted on a piezo using a lens in cat's eye configuration. The light reflected at the mirror is then coupled back into the fiber and fed into the laser diode.

The polarisation optics which consists of a quarter wave plate, a polarising beam splitter (PBS) and a polariser are used to adjust the feedback ratio p. The photodiode placed left of the 90:10 BS is used to monitor the feedback power. At a fixed external feedback path length of 2 m, the feedback power ratio p is varied from -50 dB to -30 dB. The effect of the optical feedback on the linewidth of bare DBR laser is characterized using a delayed self-heterodyne (DSH) setup described in the next chapter.

CHAPTER 3

Linewidth Measurement

The coherence of the optical phase lock used for driving the Raman transitions depends strongly on the Lorentzian linewidth of the laser resulting from the white frequency noise. With the intent to decrease this contribution, an external optical feedback path was set up. The spectral properties of any laser are quantified either by their optical line shape and associated linewidth or in terms of power spectral density (PSD) of their frequency noise $S_\nu(f)$. Various measurement techniques can be used for evaluating the phase noise of a laser. For example, a direct heterodyne measurement between the laser under test and a reference laser which has negligible or similar phase noise as the test laser [35, 36]. Or a frequency-to-intensity conversion through a frequency discriminator, such as an atomic absorption line or reference cavity [35–37]. Since neither another laser source at 770 nm nor a narrow linewidth reference cavity (linewidth < 20 kHz) were available, an alternative heterodyne measurement technique was set up, where the reference laser is replaced by a time delayed and frequency shifted part of the laser under test. This delayed self-heterodyne (DSH) [20] method was used to characterise the spectral properties of the DBR laser subject to controlled optical feedback. This chapter describes the general experimental DSH setup, the offset lock and the analysis of the recorded spectra.

It is known that DBR lasers are not only affected by white frequency but also by the flicker $(1/f)$ and random-walk $(1/f^2)$ frequency noise at low frequencies [21–23]. An analytical expression describing the correlated DSH signal that includes these high order frequency noise is hard to derive, therefore, the obtained spectra were fitted with numerically simulated spectrum based on [24]. A detailed analysis of all the noise components and their respective linewidth of the set up DBR laser system using the simulation-based fitting routine is presented in this chapter.

3.1 Delayed Self Heterodyne Measurement

DSH is based on recording a beat response of the laser with itself after one part of the laser is delayed by τ_o and the other frequency-shifted by δ_f using an acoustic-optic modulator (AOM). The two beams are then recombined on a photodiode. The spectrum of the beat signal as analysed with a electrical spectrum analyser (ESA) can be used to extract linewidth of the laser. The intensity $I(t)$ detected on the photodiode (PD) along with the phase noise $\phi(t)$ can be written as [38, 39]

$$I(t) = I_o \cos\Big(2\pi\delta_f t + 2\pi(f_s + \delta_f)\tau_o + \phi(t + \tau_o) - \phi(t)\Big) \tag{3.1}$$

where I_o is the amplitude of the photocurrent and f_s is the laser frequency. The power spectral density (PSD) of the DSH signal is then defined as the Fourier transformation of the Autocorrelation function (ACF)

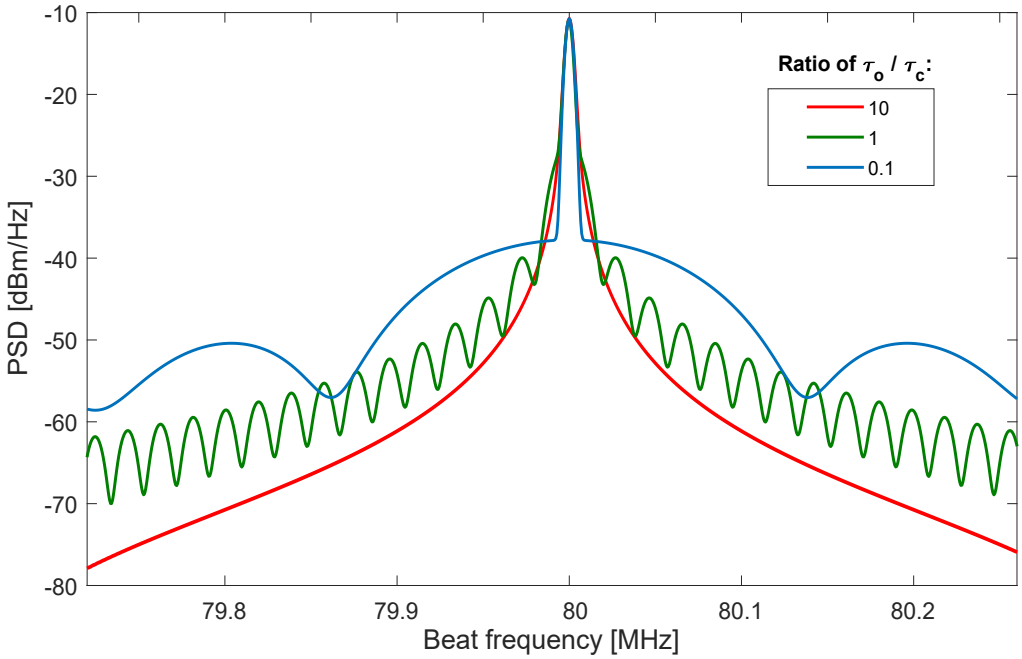

Figure 3.1: Numerically simulated DSH spectrum for different ratio of delay times τ_o and coherence time of the laser τ_c. Note: For better visualisation, the y-axis is scaled for each curve. Only the lineshape matters.

of the photocurrent. The ACF in case of white frequency noise can be expressed as [39]

$$F(\tau) = \cos\left(2\pi\delta_f \tau\right) \begin{cases} exp(-2\pi^2 k_w|\tau|), & \tau < \tau_o \\ exp(-2\pi^2 k_w \tau_o), & \tau > \tau_o \end{cases} \tag{3.2}$$

where $k_w = \delta\nu/\pi$ is the single-sided white noise coefficient in Hz^2/Hz with $\delta\nu$ being the intrinsic linewidth. The PSD of the DSH signal is then derived by Fourier transformation of Eq. 3.2 [39]:

$$S_I(\Delta f, \tau_o) = \frac{\exp(-2\pi^2 k_w \tau_o)}{2\pi}\delta(\Delta f) + \frac{k_w}{\pi^2 k_w^2 + \Delta f^2}\{1 - \exp(-2\pi^2 k_w \tau_o)[\cos\left(2\pi\Delta f \tau_o\right) + \frac{\pi k_w}{\Delta f}\sin\left(2\pi\Delta f \tau_o\right)]\} \tag{3.3}$$

Here, $\Delta f = f - \delta_f$ is the relative frequency referred to the central frequency δ_f of the beat signal. The equation above indicates that as the delay time τ_o is increased, the power in the spectrum shifts to the modified Lorentzian from the delta function peak until the power spectrum becomes a pure Lorentzian function. The pure Lorentzian function (red curve in Fig. 3.1) corresponds to delay times much longer than the coherence time of the laser ($\tau_o >> \tau_c$) such that the two beams are completely uncorrelated. In this particular case, the linewidth is the full width at half-maximum (FWHM) of the spectrum. However, when the delay time is comparable to the coherence time of the laser ($\tau_o \approx \tau_c$), the residual coherence between the two interferometer paths results in a sharp Lorentzian at the AOM frequency along with periodic ripples on the wings (green curve in Fig. 3.1). The ripples are the consequence of the coherent

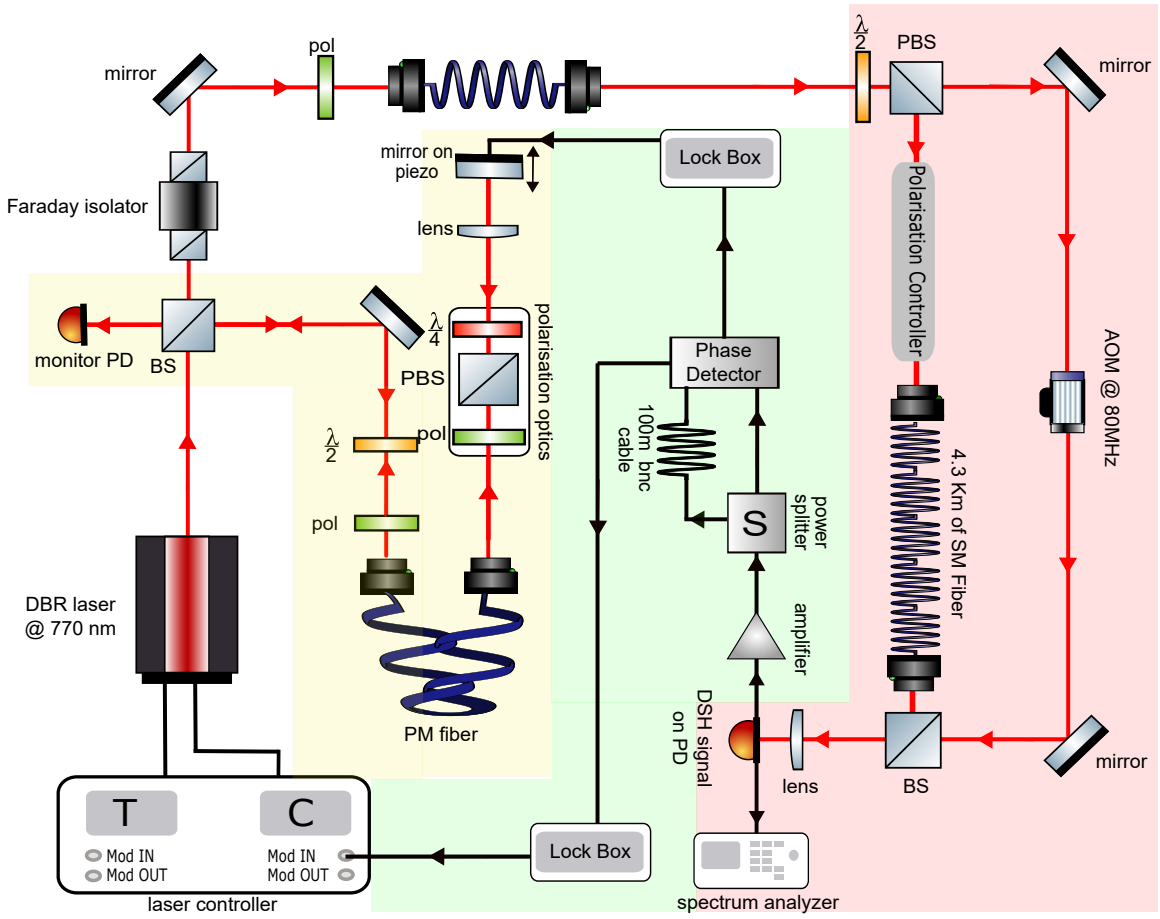

Figure 3.2: Highlighted in yellow is the 2m long external optical feedback path which couples emitted laser light back into the diode. Highlighted in red is the DSH setup used for measuring the linewidth of the DBR laser after the external optical feedback is active. The free space optical feedback path can by slow drifts cause a smearing of the DSH signal. So, a slow frequency offset lock was setup to record DSH spectra [41]. The frequency offset locking scheme is highlighted in green.

superposition between the noise from the two interferometer path. The depth of the ripples on the wings of the lineshape depends on the laser linewidth. For delay times shorter than the coherence times ($\tau_o << \tau_c$), the spectrum is a delta function peak sitting on a modified Lorentzian pedestal (blue curve in Fig. 3.1). The peak in the blue curve Fig. 3.1 is not a delta function because the simulated spectrum is convoluted with the response function of the ESA, hence finite width of the central peak. The linewidth is extracted by fitting the modulated Lorentzian pedestal [40].

3.2 Experimental Setup

Fig. 3.2 shows the complete experimental setup, highlighted in yellow is the external optical feedback path, the DSH setup is highlighted in red and the frequency offset lock, highlighted in green. In the following section we focus on the DSH setup. The output of the DBR laser, when it enters the DSH setup is divided in two parts using a polarising beam splitter (PBS) and the transmitted and reflected power

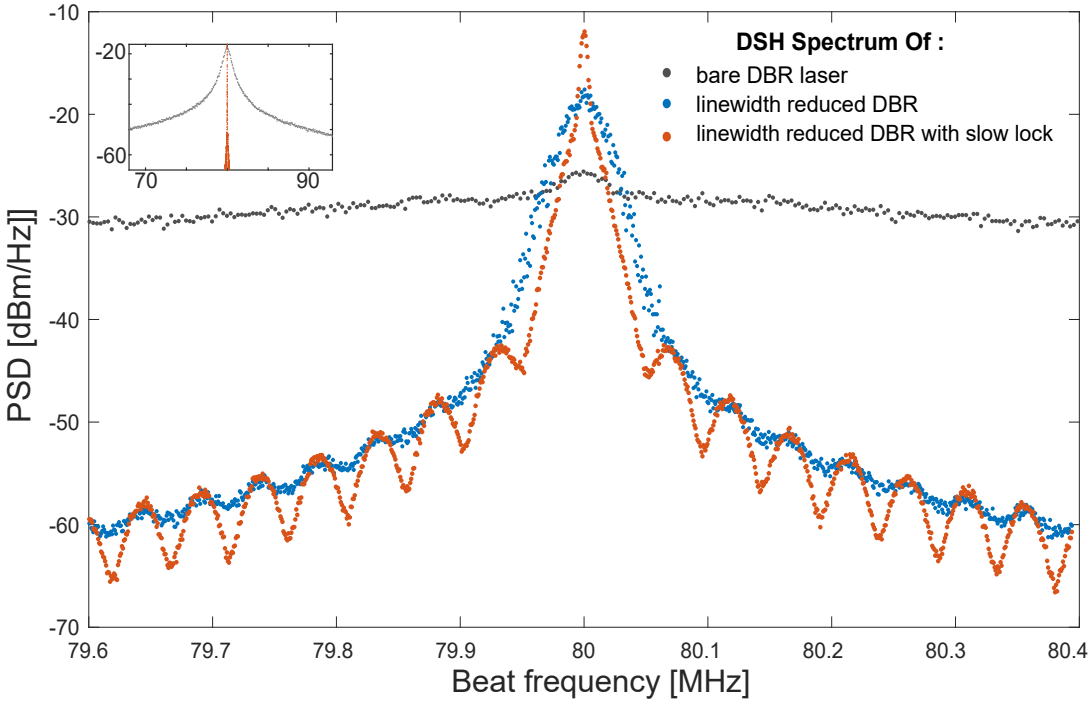

Figure 3.3: In grey is the DSH spectrum of the bare DBR laser with Lorentzian linewidth of 736.8 kHz (also shown in the inset on the left-hand side). In blue is the DSH spectrum of the DBR laser subject to optical feedback of $p = -44$ dB but when the slow frequency offset lock is not engaged. Once the slow frequency offset lock was active, distinct ripples on wing and sharper central peak appear as seen in the orange DSH curve.

is adjusted using a $\lambda/2$ plate placed before the PBS. One part of the laser is then frequency-shifted by 80 MHz using an acoustic optical modulator (AOM) and the other part of the laser is fiber-coupled into a 4.3 km long single-mode fiber. To ensure that the polarisation of the two interfering beams is same, a 3-paddle manual polarization controllers (3-PPC) is used. A 3-PPC consists of single mode fiber wrapped around three spools to create three independent wave plates ($\lambda/4, \lambda/2, \lambda/4$). The fast axis of the fiber is in the plane of the spool, stress-induced birefringence allows an arbitrary input polarization state to be adjusted by rotating the paddles [42]. The two beams are then combined on a photodiode (PD) and the resulting beat spectra is recorded on a spectrum analyser. The blue curve in Fig. 3.3 shows the recorded DSH spectra when the feedback power ratio was tuned to -44 dB. It is a power average of 50 traces recorded at a resolution bandwidth of 2 kHz.

The long external feedback path (highlighted in yellow in Fig. 3.2) consists of free space components like the quarter wave plate and a free floating external mirror mounted on a piezo. These free space components are easily affected by low-frequency acoustical noise. The frequency of the any laser subject to optical feedback is very sensitive to feedback phase as seen in Fig. 2.4, the plots for numerical solution of rate equations. Therefore, in the case when the end-mirror of the external optical path is not stabilised, the frequency of the laser is continuously drifting.

Due to the 4.3 km path imbalance between the two arms in the DSH, the frequency drift of these signals is delayed with respect to each other. The shorter arm contains the "new" laser frequency f_s whereas the delayed signal has the "old" frequency f_l solely by the virtue of the time it takes for the signal to travel to the PD. The beat signal is now centred at $\delta_f + (f_s - f_l)$, where $\Delta f_{net} = f_s - f_l$ is net drift of the DSH

signal. This net drift Δf_{net} was measured with the ESA to be ~ 50 kHz. Since the final recorded DSH spectrum are a power average over 50 traces, the frequency jitter smears out the ripples and broadens the central peak leading to deceptive linewidth estimation.

To avoid this smearing by low-frequency drifts and to measure the actual linewidth of the DBR laser subject to the optical feedback, the end mirror of external feedback path was locked using a slow frequency offset lock.

3.2.1 Frequency Offset Lock

Frequency offset lock makes use of the frequency-dependent phase shift experienced by a signal when it propagates through a delay line of coaxial cable [43]. The frequency offset locking scheme used in our experiment can be seen in Fig. 3.2, highlighted in green. It uses the interferometric signal from DSH signal to generate a correction signal for stabilising the external feedback path being a self-referenced or reference-less locking technique [41].

The large optical path imbalance in the DSH setup provides the laser's present and past output. The comparison of these two provides an estimate on the frequency drift Δf_{net}. To measure the drift the DSH signal is amplified and split into two equal parts using a power splitter. The two signal are recombined on a phase detector, after one part has been delayed by 100 m of BNC coaxial cable. The resulting output voltage V of the phase detector varies as $\cos(\phi)$ where $\phi = 2\pi(\Delta f_{net} + \delta_f)\tau$, where τ is the delay time introduced by the 100 m cable.

The zero crossings of the signal provide the error signal for locking the frequency drift using a servo loop. A longer delay line would enhance the resolution, but reduce the capture range of the lock. In our experiment, the length of the electrical delay line (BNC coaxial cable) was adjusted such that the zero crossing of the error signal falls at the AOM frequency at 80 MHz. The lock had a capture range of 10 MHz and a frequency resolution of 0.3 mV/kHz in the linear region around the locking point.

The error signal is processed via a slow servo circuit with integral gain and applied to the piezo, stabilising the length of the external optical feedback path. The correction signal was also applied to the current of the laser diode via the modulation port available on the laser controller. The locking bandwidth of the lock is a few kHz.

The orange and the blue curve in Fig. 3.3 are the DSH spectrum of the DBR laser when the feedback power ratio was tuned carefully to −44 dB. However, the former is recorded with an active frequency offset lock. With such a locking scheme in place, DSH data was recorded for feedback powers ranging from −48.8 dB to until the laser showed multi-mode behaviour.

3.3 Linewidth Analysis of the DBR Laser

We first briefly review the general relationship between the frequency noise spectral density $S_\nu(f)$ of a laser and its line shape and then discuss the PSD of the phototcurrent produced in the heterodyne detection. The electric field $E(t)$ of a single-mode laser with phase noise $\phi(t)$ and frequency ν_o can be written as

$$E(t) = E_o \exp\big(i(2\pi\nu_o t + \phi(t))\big) \tag{3.4}$$

Given $S_\phi(f)$ and $S_\nu(f)$ are the single-sided phase and frequency noise PSD, respectively, one can calculate the autocorrelation function $\mathrm{T}_E(\tau) = \langle E^*(t)E(t+\tau)\rangle$ as follows [44, 45],

$$\mathrm{T}_E(\tau) = E_o^2 \exp\left(i2\pi\nu_o\tau\right) \exp\left(-2\int_0^\infty S_\nu(f)\frac{\sin^2(\pi f\tau)}{f^2}\,df\right) \tag{3.5}$$

$\Delta\nu(f) = \nu - \nu_o$ is the laser frequency deviation around its average value ν_o. According to the Wiener–Khintchine theorem, the laser spectrum is given by the Fourier transform of the autocorrelation function and can be written as

$$S_E(\nu) = 2\int_{-\infty}^{\infty} \exp(-i2\pi\nu\tau)\mathrm{T}_E(\tau)\,d\tau \tag{3.6}$$

The integral in Eq. 3.6 can be fully solved analytically for white noise frequency noise $S_\nu(f) = k_w$ only, where k_w is the single-sided noise coefficient in $\mathrm{Hz}^2/\mathrm{Hz}$ leading to a Lorentzian lineshape with full width half maximum FWHM = $k_w\pi$ [44]. Typically, lasers are also affected by flicker $(1/f)$ or random-walk $(1/f^2)$ frequency noise which leads to non-analytical lineshapes that can only be obtained numerically.

In the experiment, the PSD of the DSH signal is obtained by Fourier transformation of the autocorrelation function of the detected photocurrent. As discussed in Section 3.1. The analytical expression (Eq. 3.3) includes contribution of the white frequency noise only which was used in Fig. 3.4 to fit a spectrum with $p = -44.4$ dB. The analytically spectrum either fits well to the central peak or the ripples on the wings. The Lorentzian linewidth predicted from such a fit is ~ 5 kHz, which is an over-estimated value as we find out later.

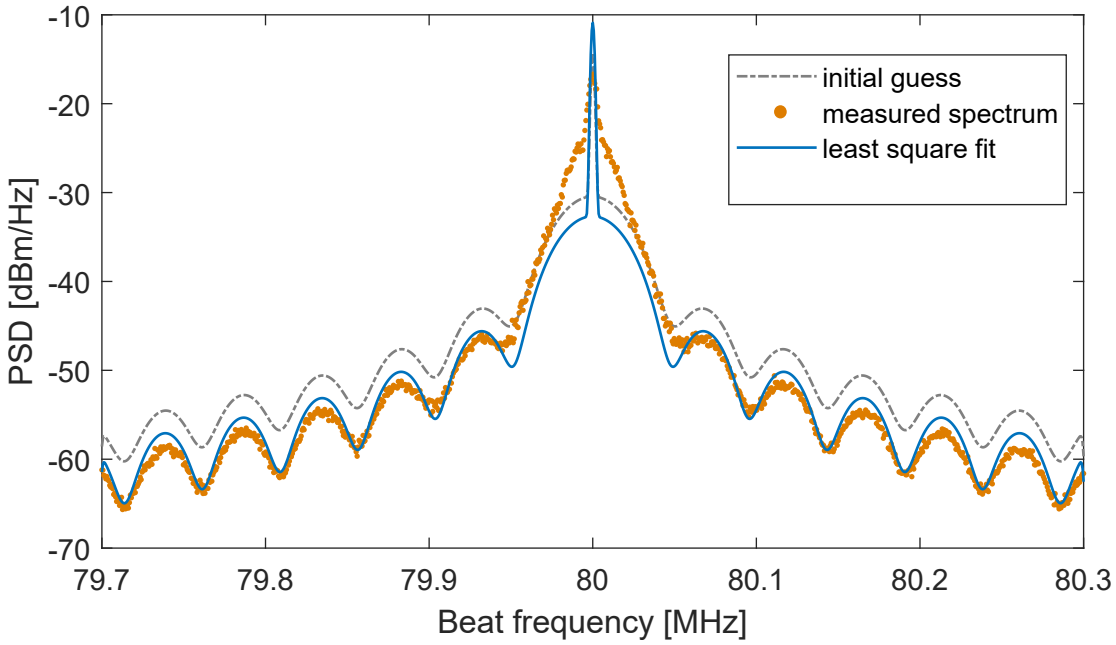

Figure 3.4: DSH spectrum at p = -44.4 dB fitted using the analytical expression (Eq. 3.3) which includes contributions from white frequency noise only. The estimated Lorentzian linewidth based on the fit is 5.093 kHz

Since there is no analytical expression for the PSD of DSH spectra including higher order frequency noise available, a numerical simulation approach to reproduce DSH spectra as in [24] was used to analyse the different noise contributions.

3.3.1 Phase Noise in Lasers

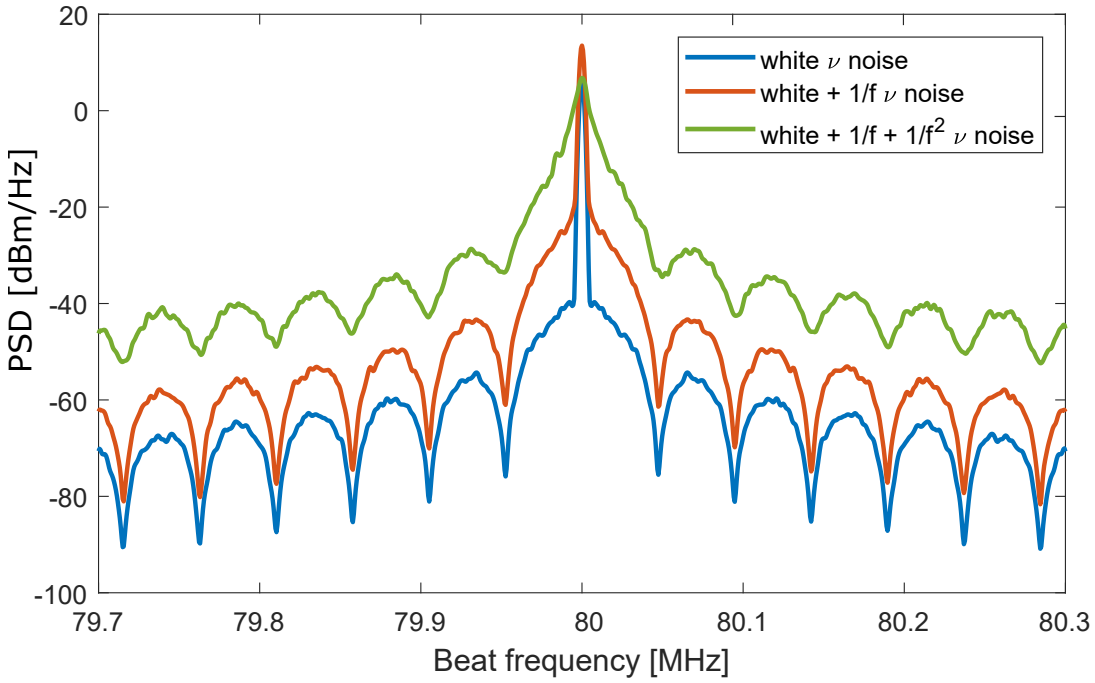

Figure 3.5: Numerically simulated DSH spectra to illustrate the effect of higher order frequency noise on DSH spectrum.

The phase noise of laser specially relevant to DBR lasers and their physical origin is described below. Laser phase and frequency noise power spectral density $S_\phi(f)$ and $S_\nu(f)$ are commonly used to quantify the phase/frequency noise power distribution over frequency. The most common noise types that are included in the analysis of laser noise processes exhibit a $1/f^\alpha$ ($\alpha = 0, 1, 2$) dependence of S_ν. The full frequency noise PSD can therefore be described by,

$$S_\nu(f) = f^2 S_\phi(f) = k_w + \frac{k_f}{f} + \frac{k_r}{f^2} \tag{3.7}$$

where k_w, k_f and k_r are the noise coefficients of the white, flicker and random-walk noise respectively. $S_\nu(f)$ and $S_\phi(f)$ are measured single-sided in the units $\mathrm{Hz}^2/\mathrm{Hz}$ and $\mathrm{rad}^2/\mathrm{Hz}$.

White frequency noise

White frequency noise in a laser results from spontaneous emission events [12]. The single-sided frequency noise PSD $S_\nu(f)$ for a pure white frequency noise is flat in frequency, and gives rise to the well-known Lorentzian lineshape described by the Schawlow–Townes–Henry linewidth [11, 12]. This linewidth component is inversely proportional to the output power of the laser. However, at high power the laser linewidth does not approach zero because of additional noise sources in a laser.

If a laser is dominated only by white frequency noise, the lineshape of a correlated DSH spectrum would be the blue curve in Fig. 3.5. With a sharp delta peak sitting on a pedestal and periodic ripples on the Lorentzian wings.

Flicker frequency noise

The carrier fluctuations introduced by surface and interface recombination leads to flicker noise [46, 47], whose single-sided frequency noise PSD $S_\nu(f) \sim 1/f$. This $1/f$-type frequency noise is dominant in low frequency region ~200 kHz to 10 MHz, is almost independent of the output power [48], and gives rise to the residual linewidth of a laser at high power. An exact expression of the line shape cannot be obtained, and different approximations have been proposed to describe the resulting spectrum [44, 48]. The lineshape is approximated to a Gaussian around the central frequency of the laser. The combined contribution of white noise Lorentzian line shape and $1/f$-noise Gaussian line shape is a Voigt profile.

The result for a simulated DSH spectrum for a laser with both white and $1/f$-type frequency noise is shown in orange curve Fig. 3.5, characterised by the broadening of the central pedestal and decreased height of the ripples on the wings of the spectrum.

Random-walk frequency noise

Random-walk frequency noise is often reported for DBR lasers [21–23]. The single-sided frequency noise PSD for this noise $S_\nu(f)$ shows $1/f^2$. The physical origin is attributed to the design of DBR lasers which differs from a conventional Fabry Perot cavity based laser. DBR lasers have separate passive tuning sections placed outside the active region of the laser cavity. Thus, besides the injection-recombination $1/f$-type noise, the carrier density fluctuations in the tuning regions can have large noise contributions [22, 23].

A simulated DSH spectrum that includes white, $1/f$-type and $1/f^2$ frequency noise is shown in green in Fig. 3.5. The $1/f^2$ frequency noise obscures the central peak in the DSH spectrum slightly different from white and 1/f frequency noise. The features of the lineshape simulated with contributions of all three frequency noise resembles closely to the measured DSH spectra.

3.4 Simulation-based Fitting Routine

The simulation-based fitting based on [24] to analyse the DSH signal by numerically simulating spectra includes contributions from higher order frequency noise also. The flow chart in Fig. 3.6 summarises the numerical simulation.

The goal of the simulation based-fitting routine is to emulate the recorded spectra by a simulation of the the photodiode signal (Eq. 3.1) with well-known noise contributions. For this, first a phase noise sequence $\phi(t)$ is generated (Section 3.4.1) by superposition of a white $\phi_w(t)$, a flicker $\phi_f(t)$ and a random-walk $\phi_r(t)$ frequency noise source as:

$$\phi(t) = A_w \phi_w(t) + A_f \phi_f(t) + A_r \phi_r(t) \tag{3.8}$$

A_w, A_f, A_r are the noise amplitudes of the corresponding noise sources. These are also the parameters that are optimized to fit the numerically simulated spectrum to the experimental data. Each of the $1/f^m$ (m=0, 1, 2) noise is produced by spectrally filtering white noise (Section 3.4.2). The fourth parameter that is optimized is the signal strength I_o.

The PSD of the heterodyne signal (Eq. 3.1) is calculated by the Welch method (Section 3.4.3) and convoluted with the response function of the ESA. The fitting parameters $[I_o, A_w, A_f, A_r]$ are optimised using the Nelder-Mead Simplex search (Section 3.4.4). Once the error between the numerically simulated and the measured spectra converges, we calculate the three noise coefficient k_w, k_f and k_r from the

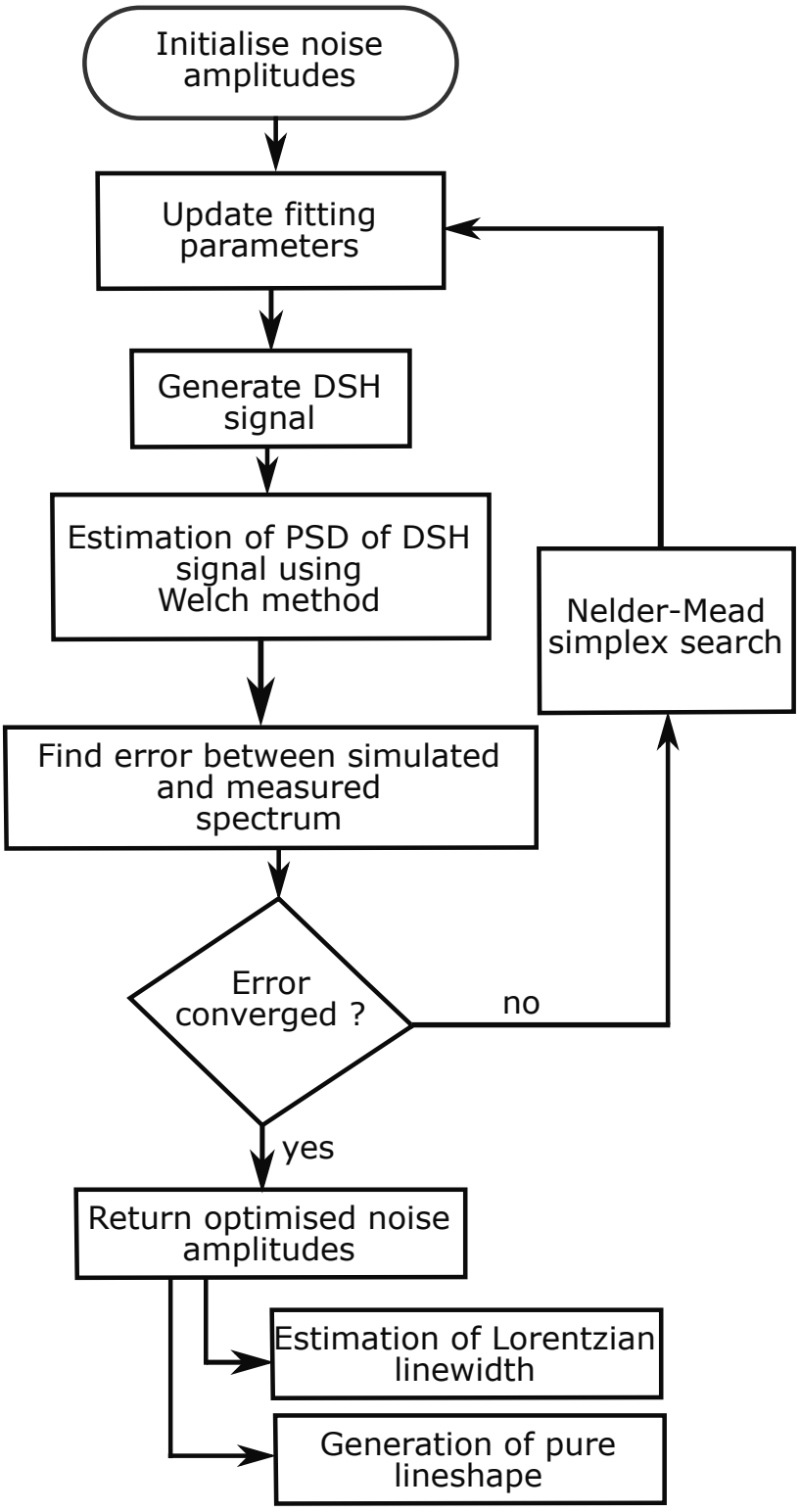

Figure 3.6: Flowchart of the steps used in the simulation based fitting routine [24].

optimised noise amplitudes (Section 3.6) . Finally, an estimate on the linewidth corresponding to each frequency noise can be made, presented in Section 3.7.

3.4.1 Generating Discrete-time Signal

In order to generate the continuous photodiode signal or the phase noise signal numerically in Matlab®, we use a technique called *sampling*. *Sampling* is the process of converting a continuous-time signal into a discrete-time signal. The signal is converted by finding its value at uniformly spaced points in time. The spacing between two consecutive samples is called the *"time sampling constant"*, determined by the delay time (τ_o) [24] and the sampling theorem. We start by re-writing the continuous phase noise sequence (Eq. 3.8) in discrete-time domain,

$$\phi(mT_s) = A_w\phi_w(mT_s) + A_f\phi_f(mT_s) + A_r\phi_r(mT_s) \tag{3.9}$$

where $m \in 1, 2, ..., n$ is the integer length of the full noise vector or the associated DSH signals, chosen as $n = 10^7$ throughout the data analysis using this simulation-based fitting. The upper-limit of the value is strictly based on computation capabilities of the computing machine. A smaller number of samples leads to a more noisy spectrum, making it harder to fit them to experimental data. The chosen length provides a good trad-off of accuracy compared to the necessary computing time for the ressources of a common PC.

T_s is the *time sampling constant* chosen as $T_s = 1/sigsamp * \delta_f$, where δ_f is the beat frequency of the DSH signal given by the AOM. *sigsamp* determines how many points are samples during an oscilltion of the beat signal. A large value of *sigsamp* implies finer sampling of the signal. The smaller over all time (n*T_s) however results in a noisier spectrum for a fixed n. For the presented analysis of spectra (n, sigsamp, δ_f) = (10^7, 5, 80 MHz) was used.

3.4.2 Generating white, $1/f$ and $1/f^2$ Frequency Noise Sources

Each of the noise component can be generated by using a spectral filter on a flat spectrum, i.e., dividing a flat spectrum locally by f^s, where $s = 2, 3, 4$ for white, flicker and random-walk noise, respectively. We do so in Matlab by first generating a time vector of length n with Gaussian noise using the `randn` command giving the time trace of a spectrally flat random process. We perform a Fourier transform of it using the in-build `fft` command to be able to apply the spectral filters. Finally, an inverse Fourier transform is applied to retrieve the corresponding time sequences. Each of the noise components is generated from a separate random trace.

3.4.3 Welch Method

One of the most important steps in the simulation is calculating the PSD of the heterodyne signal or of the phase noise. PSD of a signal x can be calculated as

$$S_x(f) = \mathcal{FT}(x)\mathcal{FT}(x)^* = |\tilde{x}(f)|^2 \tag{3.10}$$

where $\mathcal{FT}$ and $\sim$ denotes the Fourier transform. To compute the PSD in the simulation, we use the Welch method [49], which reduces the noise of the PSD by averaging. It is based on Bartlett's method which involves dividing the signal in K subsets of length L, computing periodograms of these subsets, and averaging over these periodograms. For the Welch method the K subsets of length L are overlapped by D points (Fig. 3.7). For the simulation we chose, D = L/2 i.e. 50% overlap.

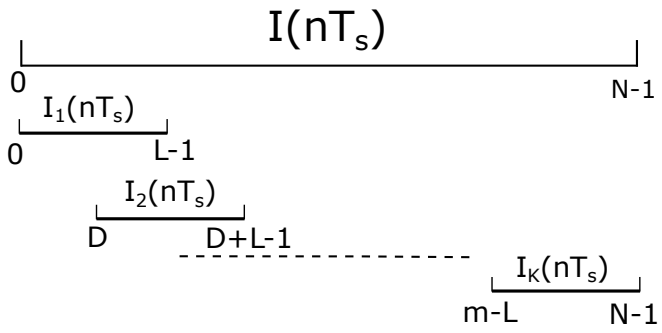

Figure 3.7: Illustration of segmentation of a signal in K subsets of length L with $D = L/2$, i.e. 50% overlap in Welch method [49].

The overlapped segments are then windowed by a window function $w(nT_s)$ in the time domain. The type of window function used in the simulation is discussed in the next section. The periodogram is calculated for each of the segment, by computing the discrete Fourier transform using the FFT command in Matlab, and then computing the squared magnitude of the result. Finally, the PSD of the DSH signal is obtained by averaging the PSDs of K subsets,

$$S(l) = \frac{1}{\mathrm{K}} \sum_{m=1}^{K} \frac{\left|\sum_{n=0}^{L-1} I(nT_s) w(nT_s) e^{-i\frac{2\pi}{L}nl}\right|^2}{\sum_{n=0}^{L-1} w(nT_s)^2} \tag{3.11}$$

where $w(nT_s)$ is the normalised window function.

Window Function

Matlab's `fft` command computes the discrete Fourier transform (DFT) of the finite data samples. These samples cut the signal at their boundaries, which appears as a discontinuity of the DFT, if the signal period is not an integer fraction of the segment length. The discontinuities appear as high-frequency components which were not present in the original signal. This causes the energy to leak into other frequencies, also called spectral leakage. In order to reduce spectral leakage window functions are used.

Windows are weighting functions that are applied to each segment in time domain before applying the DFT. These functions are applied as multiplicative weights to the data to reduce the order of discontinuity. Most of the window functions start near or at zero, then increase to a maximum at the center of the time series and decrease again afterwards symmetrically. Thus, reducing the discontinuity. Different window functions affect attributes of the resulting signal in frequency domain differently; for example, width of the peak, amplitude accuracy or resolution [50].

For our simulation, we chose the Hann window (Eq. 3.12), named after the Austrian meteorologist Julius von Hann. This window belongs to $\cos^{\alpha}(X)$ family, where the parameter α is an integer. The general form of this window function for finite Fourier transform is

$$w(n) = \cos^{\alpha}\left[\frac{n}{N}\pi\right], \qquad n = -\frac{N}{2}, .., -1, 0, 1, ..., \frac{N}{2} \tag{3.12}$$

$\alpha = 2$ is the Hann window, also known as raised cosine or Hanning and is shown in Fig. 3.8. This window has a wide peak but low side lobes, touching zero at both the end of the signal, removing all the

discontinuity. Side note: The charm of a Hann window with 50% overlap is that all points in the full time series contribute at the end with equal weight (except the first part of the very first segment and the last part of the very last one).

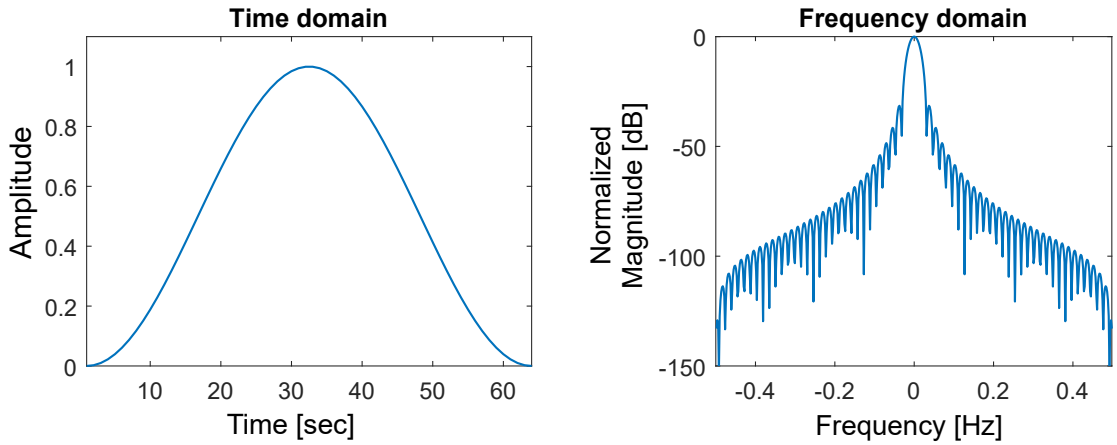

Figure 3.8: Hann window in time and frequency domain.

3.4.4 Nelder-Mead Simplex Search

The method used for optimizing the simulated spectrum is the *downhill simplex method* developed by John Nelder and Roger Mead in 1965 [51]. The algorithm finds a local maximum or minimum of an objective function in a multidimensional space since it requires only function evaluations, not derivatives, the number of evaluations is smaller than gradient based searches. The method uses the concept of a *simplex*, a geometrical figure residing in N dimension, consisting of $N + 1$ points (vertices) and all their interconnecting line segments, polygonal faces, etc. For example, in two dimension, a simplex is a triangle. In three dimension it is a tetrahedron, as shown in top of Fig. 3.9.

The "geometrical nature" of this algorithm makes it easy to understand. For multidimensional minimization, we start with a N-vector of independent variables (initial guess). The algorithm then makes its own way downhill through the N-dimensional topography, until it encounters a (local, at least) minimum. The downhill simplex method starts with defining a simplex with N+1 points. One of these points is the initial guess I_o, the other N points are defined as

$$I_i = I_o + \lambda e_i \tag{3.13}$$

where the e_i's are N unit vectors, and λ is a constant which is the guess of the problem's characteristic length scale.

The downhill simplex method takes a series of steps, most steps to move away from the point where the objective function is largest ("high point") through the opposite face of the simplex to a lower point. These steps are called reflections which conserve the volume of the simplex. Fig. 3.9 shows an intial simplex, a tetrahedron with highest and lowest point marked. In Fig. 3.9, (a) shows the reflection away from the high point. The method can also expand the simplex in one or another direction to take larger steps, called reflection and expansion ((b) in Fig. 3.9). If the method after a couple of iterations of the above mentioned steps reaches a "valley floor", it contracts itself either in one direction away from the

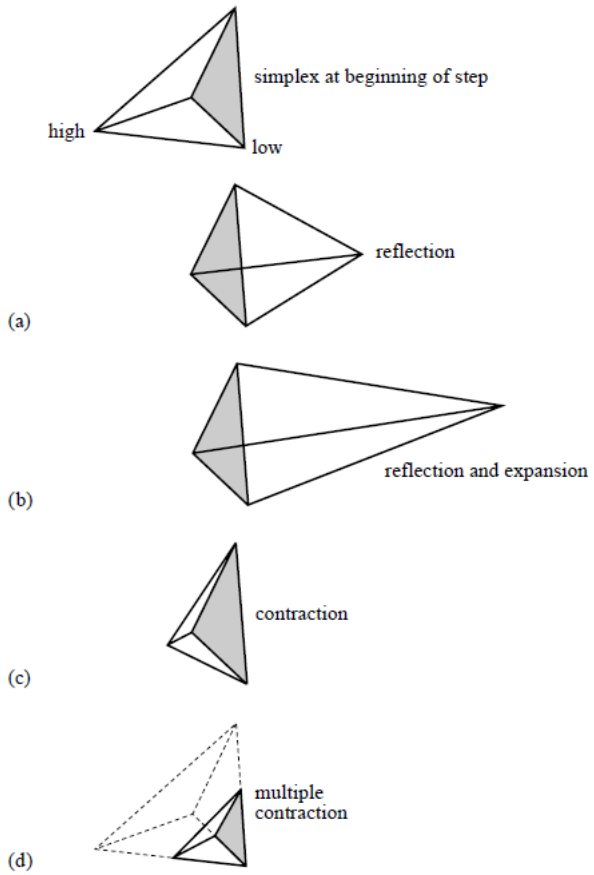

Figure 3.9: Possible step types in the Nelder-Mead downhill simplex method. In three dimension, a simplex is a tetrahedron in the parameter space, as shown, in top. To minimize the cost function in the parameter space, the simplex can perform one of the following operations at every step (a) a reflection away from the high point, (b) a reflection and expansion away from the high point, (c) a contraction along one dimension from the high point, or (d) a contraction along all dimensions towards the low point. An appropriate sequence of such steps will converge to atleast a local minimum of the objective function. Illustration from [52].

high point (contraction, (c) in Fig. 3.9) or it contracts in all directions (multiple contraction, (d) in Fig. 3.9) around its lowest points and tries to reach the valley bottom (at least a local minimum).

This method is pre-implemented in Matlab in the `fminsearch` function. The arguments of the function are the objective function $func$ and the initial parameters $A_{in} = [A_w, A_f, A_r, I_o]$. To optimize the resemblance of the simulation with the measured spectrum, the objective function chosen for the simulation is the sum of the squared residuals (SSR),

$$func = \sum_f |(S_{sim}(f) - S_{exp}(f))|^2 \tag{3.14}$$

where the index f represents all the frequencies (79.6 MHz to 80.4 MHz). S_{sim} and S_{exp} are the numerically simulated PSD (dBm/Hz) and experimentally obtained PSD (dBm/Hz) at the frequency f.

The algorithm performs a series of the steps described above to find the set of $[A_w, A_f, A_r, I_o]$ for which the objective function is minimum. Since it is also important to fit the behaviour away from the main peak in the spectrum, the optimisation is performed in log-space. Fig. 3.10 shows an optimised

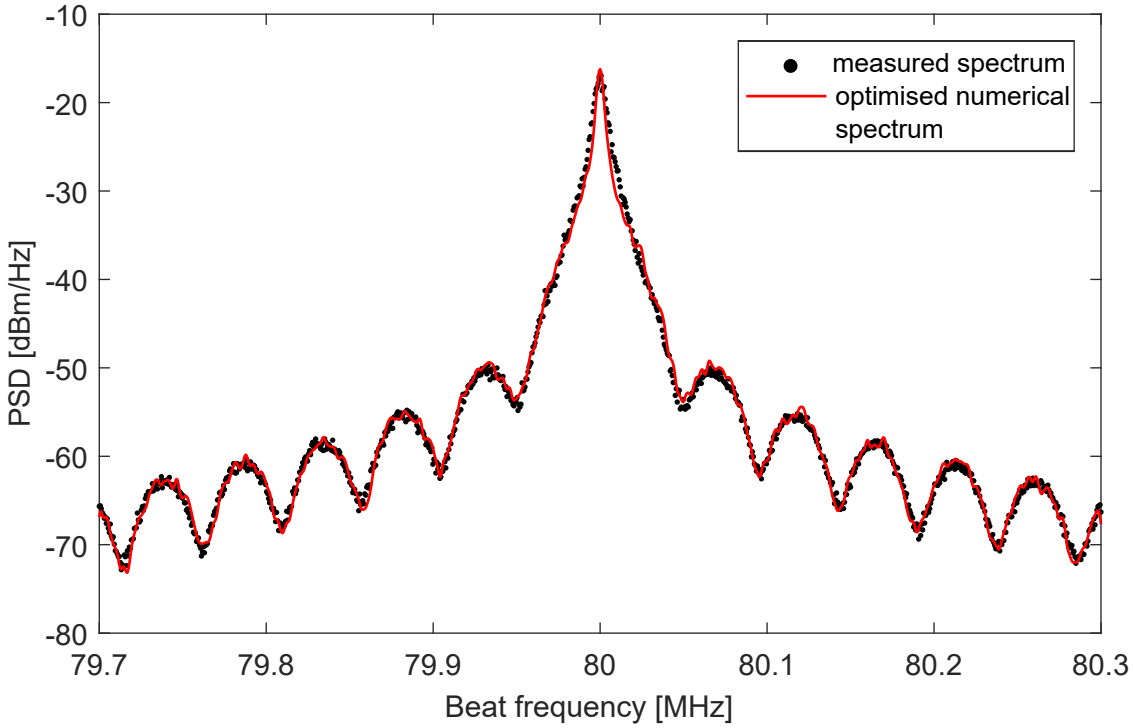

Figure 3.10: DSH spectrum at $p = -40.9\,\mathrm{dB}$ fitted using the simulation based fitting routine. The estimated Lorentzian linewidth is 0.599 kHz.

simulated spectrum.

The termination of the algorithm depends on the maximum number of function evaluations, the tolerance on the change of the value of the objective function during each step and on the size of the step itself. The termination criteria used for our simulation is discussed below.

Termination Criteria

Matlab's function `fminsearch` provides three parameters, namely `MaxFunEvals`, `TolFun` and `TolX` to terminate the algorithm. The `MaxFunEvals` is maximum number of function evaluations allowed, set to 100 for our simulation. To ensure faster convergence, the initial guess is updated manually for each dataset until the simulated spectrum is very close to the experimental spectrum. Once this is achieved, the initial parameters is fine tuned using the Nelder-Mead algorithm and 100 evaluations of the objective function is fairly sufficient.

`TolX` is a lower bound on the size of a step, meaning the norm of $(A_i - A_{i+1})$, where A_i and A_{i+1} contains the value of the initial parameters at *ith* and *(i+1)th* iteration. `TolFun` is a lower bound on the change in the value of the objective function $func$ during a step. We set both `TolX` and `TolFun` to 10^{-2}. When $A_i - A_{i+1} <$ `TolX` and $|func(A_i) - func(A_{i+1})| <$ `TolFun`, the iterations end. Fits does not necessarily yield better results for decreasing the value of both `TolX` and `TolFun`. Because of its finite sample size the simulation is noisy itself and will not fit the data increasing well. To reach better values the averaging in the simulation would need to be increased by using longer time vectors (larger values for n) which linearly increases the simulation time, being the time of just a single function evaluation in the optimization. Increased accuracy comes, therefore, at the cost of much larger fit times.

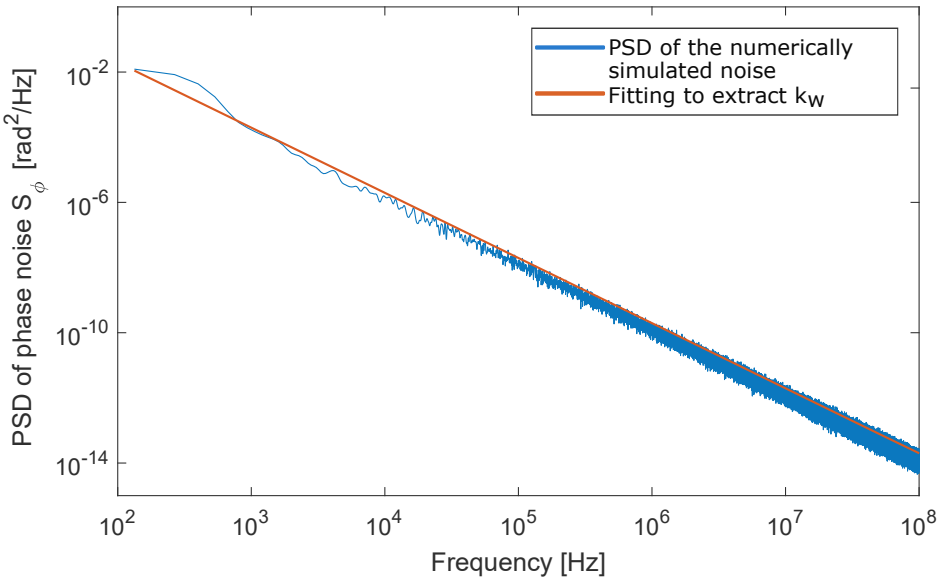

Figure 3.11: PSD of the phase noise S_ϕ with white noise source only to extract k_w.

3.5 Lorentzian Linewidth Estimation : PSD of Phase Noise

The optimized noise amplitude A_w from the phase noise sequence is used to extract the Lorentzian linewidth of the laser. We do so by computing the PSD of the phase noise $S_\phi(f)$ by including only the white noise contribution. For the feedback power =−44.4 dB, the phase noise PSD of white noise is shown in Fig. 3.11. The simulated data is fitted with

$$S_\phi(f) = \frac{k_w}{f^2} \tag{3.15}$$

where the white noise coefficient $k_w = \delta\nu/\pi$, $\delta\nu$ is the intrinsic Lorentzian linewidth of the laser. The estimated intrinsic linewidth of the laser at a feedback power ratio of −44.4 dB is 1.085 kHz. Similarly, the Lorentzian linewidth for all feedback powers ratio from the PSD of the phase noise is computed and plotted in Fig. 3.12. Each linewidth data point is an average of four independently recorded experimental traces, the error bars are the standard deviation from the mean value. Apart from the linewidths retrieved through the fitting of the white noise part of the phase noise PSD (in green), Fig. 3.12 also shows the linewidths as extracted via two other methods that are explained in the upcoming sections.

3.6 Noise Coefficients

To estimate the noise coefficient of each noise, we start with Eq. 3.7,

$$S_\phi(f) = \frac{k_w}{f^2} + \frac{k_f}{f^3} + \frac{k_r}{f^4} \tag{3.16}$$

In the simulation, the PSD of each phase noise can be evaluated separately using the Welch estimation by making use of the fitted noise amplitudes $[A_w, A_f, A_r]$ as

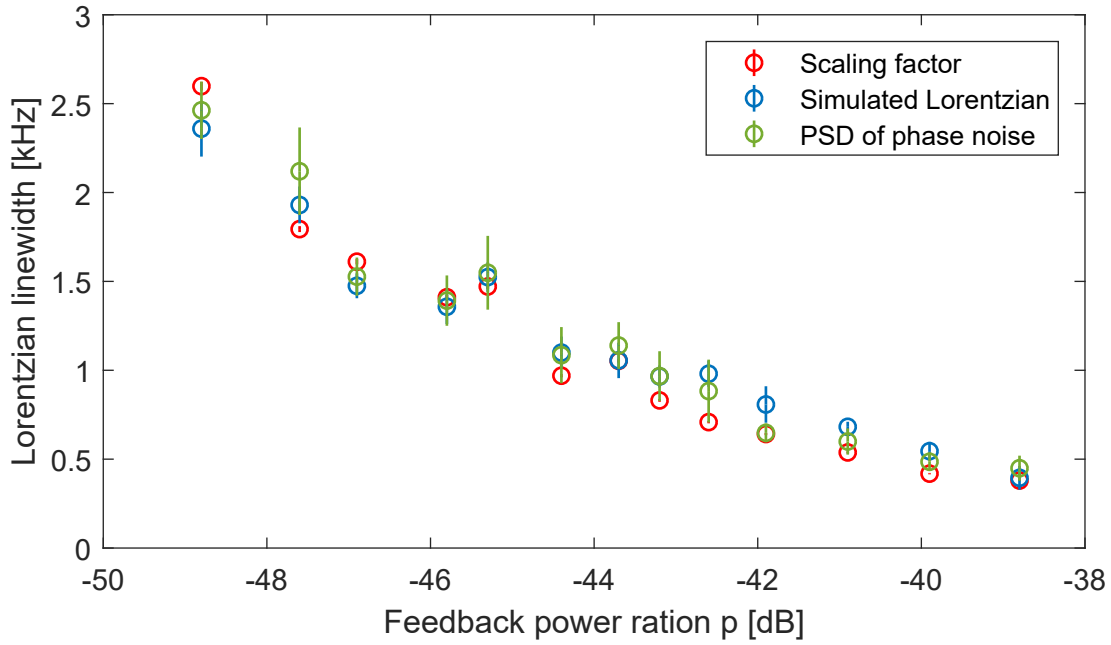

Figure 3.12: Estimated Lorentzian linewidth for increasing feedback power ratio p from three methods. The DSH measured laser linewidth derived from the three methods are comparable within the error bars.

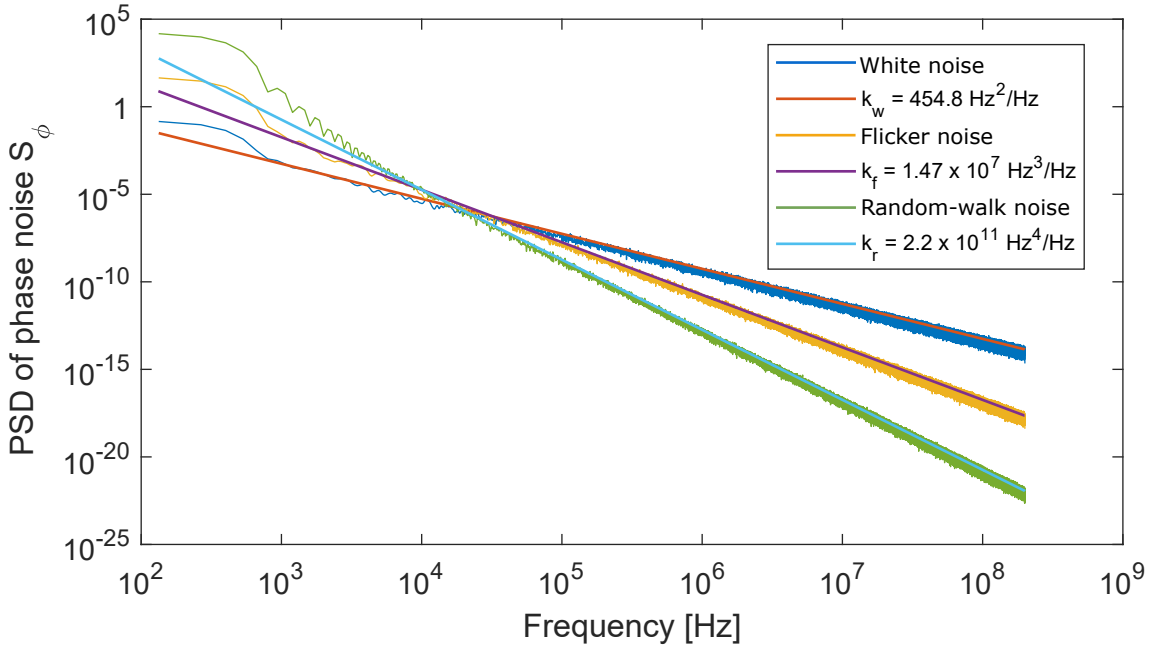

Figure 3.13: PSD of the phase noise S_ϕ for all the three noise fitted to extract k_w, k_f and k_r.

$$S_\phi(t) = A_w^2|\tilde{\phi}_w(f)|^2 + A_f^2|\tilde{\phi}_f(f)|^2 + A_r^2|\tilde{\phi}_r(f)|^2 \tag{3.17}$$

where ~ denotes the Fourier transform of the respective phase noise. Comparing Eq. 3.17 and Eq. 3.16, the noise coefficient and noise amplitudes follow a quadratic relationship

$$k_w = c_w \cdot A_w^2 \tag{3.18a}$$
$$k_f = c_f \cdot A_f^2 \tag{3.18b}$$
$$k_r = c_r \cdot A_r^2 \tag{3.18c}$$

Once the scaling factor c_w, c_f, c_r are known, the noise coefficient can be directly computed from the fitted noise amplitude.

3.6.1 Estimation of Quadratic Scaling Factors

First, we simulate the PSD of each noise independently (Fig. 3.13) and fit them using Eq. 3.16 to extract k_w, k_f and k_r for a chosen value of A_w, A_f, A_r. For a given value of noise amplitude, the computation of the PSD and the fitting to find the noise coefficient is performed 100 times to estimate the standard deviation of the fitted parameter. The same procedure is repeated for different values of A_w, A_f, A_r. Fig. 3.14 shows the quadratic scaling of noise coefficient with noise amplitude. The scaling factors c_w, c_f, c_r are computed by performing a quadratic fit for each noise. The value of the scaling factors and their confidence intervals of the fitted parameter are summarised in the table below.

Frequency noise	Scaling factor	Confidence interval
White	0.3015	[0.3001, 0.3029]
Flicker	0.1537	[0.1536, 0.1538]
Random-walk	0.0989	[0.0988, 0.0990]

The direct relation of $A_{w/f/r}$ to $k_{w/f/r}$ can then be used to extract the noise coefficients. For the Lorentzian noise, the linewidth extracted through $\delta\nu = \pi \cdot k_w$ can then be compared for both the directly fitted k_w (green points in Fig. 3.12) and the k_w extracted through the quadratic relation (red points). The extracted noise coefficients of each frequency noise type extracted via the quadratic relation are plotted in Fig. 3.15 as a function of the feedback power ratio p.

3.7 Pure Lineshape

The simulation-based fitting routine returns four fitted parameters, the amplitude of the three noise components and the signal strength. The Lorentzian linewidth of the laser is directly extracted from k_w, the white noise coefficient from the PSD of the phase noise. The analytical expression to find the linewidth arising from 1/f noise [44] is not valid in our case. And the spectral width due to $1/f^2$-noise, an analytical expression is not available. To still extract the spectral lineshape of each noise component of the laser, we used simulated spectra of a heterodyne measurement with a perfect reference.

Assume a perfect reference laser source with no phase noise operating at $\omega_p = 80\,\text{MHz}$. The electric field $E_p(t)$ of such a laser can be written as,

$$E_D(t) \propto cos(\omega_p t) \tag{3.19}$$

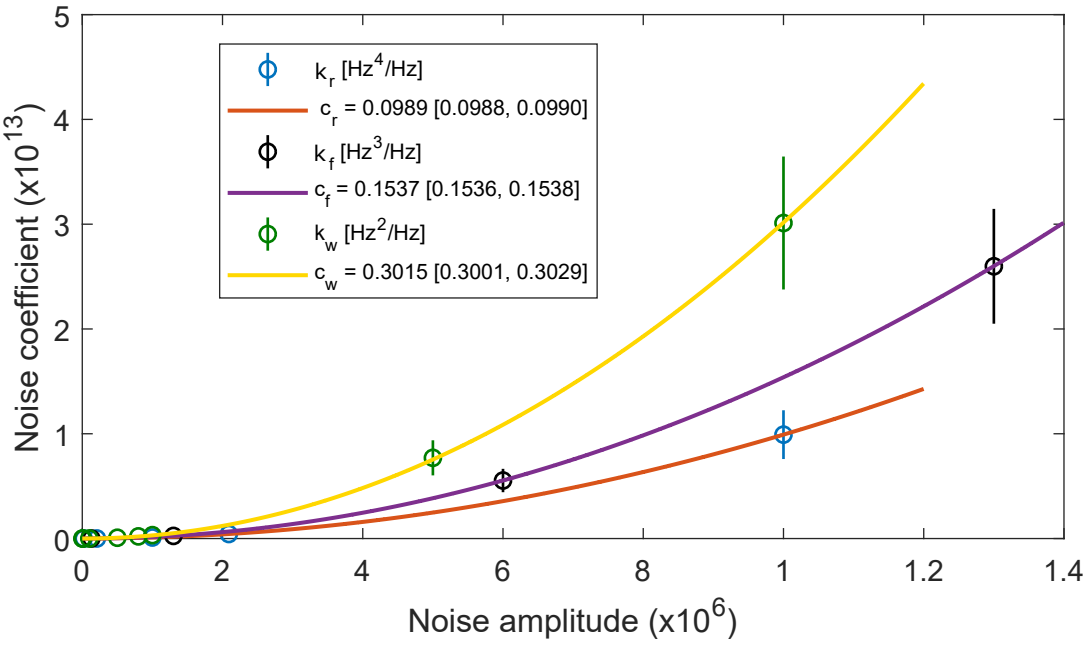

Figure 3.14: Quadratic fits of the noise coefficients with noise amplitude. Note:x and y axis of white and flicker noise have been scaled to depict all the quadratic plots in the same graph. The x and y axis for white noise are scaled by a factor of 10^4 and 10^8, whereas for the flicker noise, the x and y axis are scaled by 10^2 and 10^4.

If this perfect laser is superimposed with the DBR laser (the laser under test) with phase noise $\phi_{opti}(t)$. The total intensity $I_s(t)$ detected on the photodiode can be written as,

$$I(t) \propto \cos\Big(\omega t + \phi_{opti}(t)\Big) \tag{3.20}$$

$$\phi_{opti}(t) = A_w \phi_w(t) + A_r \phi_r(t) + A_f \phi_f(t) \tag{3.21}$$

where $\omega = 2\pi \cdot 80\,\text{MHz}$. The PSD of the signal will be square of the magnitude of the Fourier transform $S_I(f) = |\mathcal{FT}(I(t))|^2$ which for the simulation is computed using the Welch estimation. A spectral lineshape corresponding to each noise component can be simulated by setting the other two noise amplitudes to zero.

The simulated spectrum for feedback power ratio $p = -44.4\,\text{dB}$ each noise is shown in Fig. 3.16. As the white noise gives rise to a Lorentzian curve [11, 12] a pure Lorentzian can be fitted to find the Lorentzian linewidth which gives a third method to extract it as is plotted in Fig. 3.12. The linewidth of the simulated Lorentzian is comparable within the error bar to the linewidth predicted by the other two methods.

The spectrum of a laser affected only by $1/f$-noise is approximately Gaussian [44]. The simulated power spectrum is the orange curve in Fig. 3.16. A Gaussian curve is fitted to these simulated $1/f$ spectrum to estimate the linewidth of the laser generated from the flicker noise. Fig. 3.15 summarises the FWHM linewidth for each feedback power ratio p. The estimated Gaussian linewidth also decreases with increasing feedback power and is larger than the predicted Lorentzian linewidth. However, it is known that the $1/f$ noise broadens the DSH spectrum for different delay times [44]. Therefore, the estimated Gaussian linewidth is an upper limit on the real Gaussian linewidth of the DBR laser.

The noisy and broad black curve in Fig. 3.16 arises from $1/f^2$ or random-walk frequency noise. With

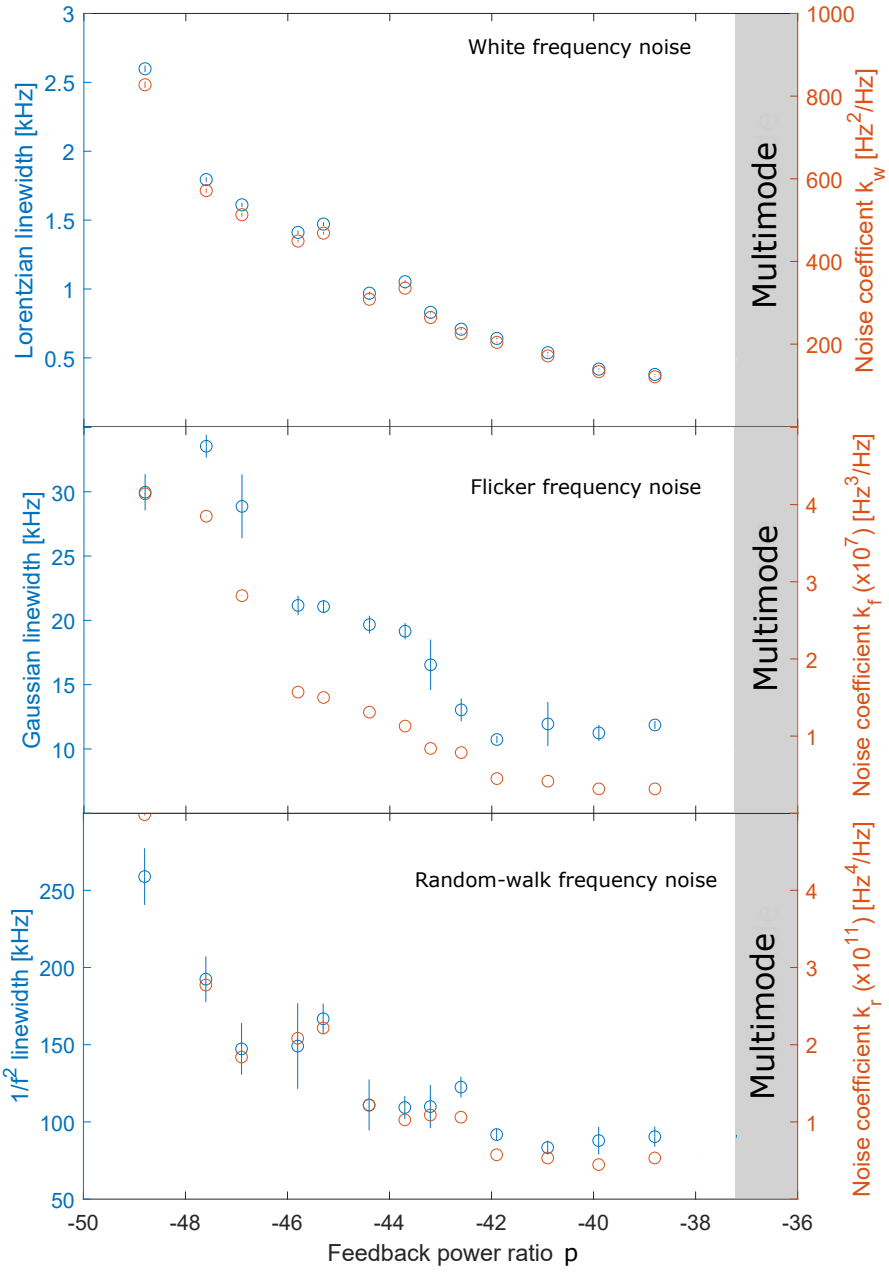

Figure 3.15: Noise coefficient (right y-axis) and associated linewidth (left y-axis) of white, flicker and random-walk frequency noise (top to bottom) as a function of feedback power ratio p. All the three noise coefficients k_w, k_f and k_r are calculated using the scaling factor c_w, c_f, c_r, respectively (Section 3.6). The Lorentzian linewidth $\delta\nu = \pi.k_w$ decreases with increasing feedback power as expected. The Gaussian and the $1/f^2$ linewidth are estimated by simulating pure $1/f$ and $1/f^2$ lineshape (Section 3.7). The error on all the estimated linewidth is the standard deviation over multiple DSH traces recorded for each feedback power.

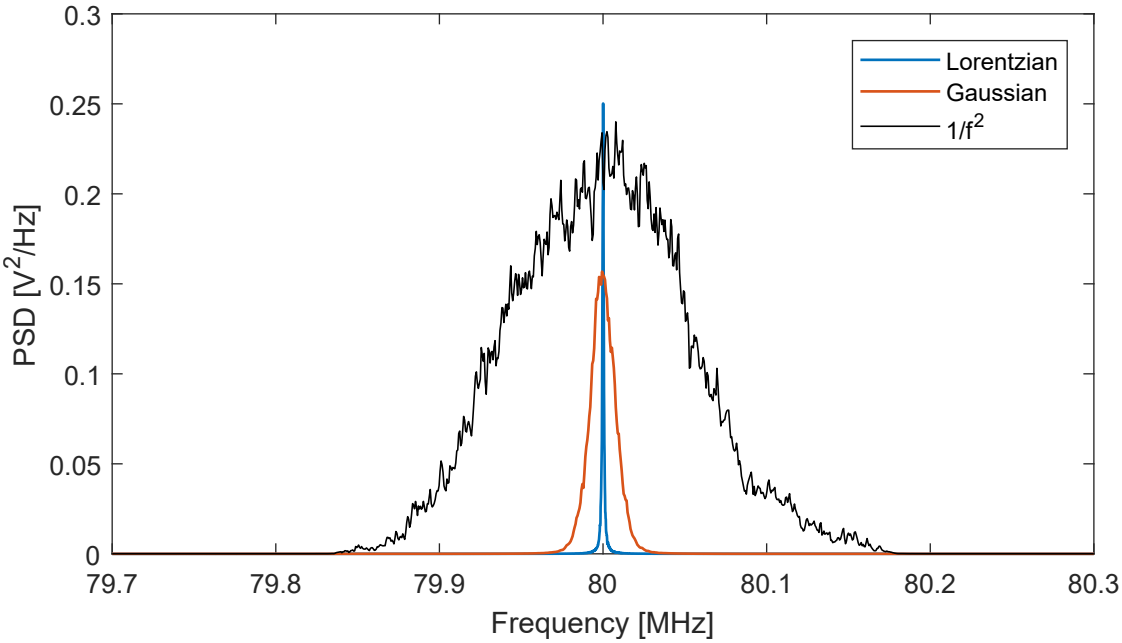

Figure 3.16: Numerically simulated lineshape of the laser for the three frequency noises, namely white, flicker and random-walk frequency noise. The white freuquency noise corresponds to Lorentzian lineshape (the blue curve) with lowest linewidth of 1.09 kHz. In orange is the approximately Gaussian linshape arising due to the flicker frequency noise with FWHM of 19.6 kHz. In grey, is the lineshape attributed to random-walk or $1/f^2$ frequency noise, averaged over 50 traces. The linewidth of this flat-top spectrum is 111 kHz.The PSD of Gaussian and $1/f^2$ spectrum is scaled by a factor of 10 and 100, respectively in order to visualise all three lineshapes in the same plot.

increasing exponent x on frequency ($1/f^x$), the noise gets slower, which means that the error phase evolves on longer timescales. Hence, longer time signal have to be analysed to retrieve a smoother spectrum or the spectrum has to be averaged over many traces. The simulated spectrum of $1/f^2$-noise in Fig. 3.16 is an average over 50 traces. The estimated full width at half maximum (FWHM) is plotted in Fig. 3.15. The $1/f^2$ linewidth also decreases with increasing p.

3.8 Conclusion

In this chapter, I presented how we acquired and analysed correlated DSH spectrum to extract the Lorentzian linewidth of the DBR laser subject to controlled optical feedback. With the simulation-based fitting routine, we could also estimate the noise coefficients and the linewidth corresponding to higher order frequency noise, especially relevant to DBR lasers. We wish to in the future make the Matlab code of the fitting routine available to everyone via MathWorks or Github.

CHAPTER 4

Carrier-free Raman Sideband Cooling

Quantum optics experiments with cold atoms and ions rely upon preparation of atoms in their motional ground state. In experiments such as our, dealing with one or few atoms, Raman sideband cooling [53] is the preferred choice for preparing the quantum motional states of these trapped atoms over other techniques like evaporative cooling [54]. It is based on driving a two photon Raman transition [55] between the hyperfine states of an atom while reducing its vibrational levels. This technique requires two lasers phase-locked with a tunable frequency offset close to the hyperfine splitting.

The blue detuned intra-cavity dipole trap created by the lock laser light in our experiment [2] serves as one of the Raman beams. To drive Raman transitions, the linewidth-reduced DBR (LR-DBR) laser is phase locked to the lock laser with an offset of ~6.8 GHz, corresponding to the hyperfine splitting of Rubidium ground states. Since the atoms are trapped at the intensity minima of the intra cavity lattice, two-photon carrier Raman transitions are suppressed [4, 5]. Using this carrier-free Raman manipulation, the atom can be cooled in all three motional dimensions.

In Section 4.1 and Section 4.2.1, I describe the setup used for locking the LR-DBR laser to the lock laser as well as the main experimental setup. With the intent to cool the atom in all the three directions with a single Raman pulse, we overlap the trap frequencies of all three dipole traps in our system. These trapping frequencies are measured and calibrated using Raman spectroscopy (Section 4.3) and finally a spectrum with all the three trapping frequencies overlapped is presented.

4.1 Raman Laser Setup

The linewidth-reduced DBR laser is phase-locked to the intra-cavity lock laser with a frequency offset that corresponds to the hyperfine splitting of Δ_{HF} = 6.8 GHz plus a variable two-photon detuning δ that can be scanned or can be set to address any desired motional sidebands.

The experimental setup for the optical phase lock loop (OPLL) is shown in Fig. 4.1. A phase frequency discriminator (PFD) is used to compare the beat signal of the two lasers to a stable reference at 6.8 GHz produced by a low noise RF source and to quantify the frequency and phase deviations. Based on these deviations, the PFD generates two error signals, a high frequency (HF) output and low frequency output (LF). The HF output is connected to a loop filter, which then applies feedback signal to as a direct current modulation on the laser diode for phase locking. The LF output is processed via a PI controller (lock box) to produce a correction signal, which is then amplified via a high voltage (HV) amplifier and applied to the piezo-mirror of the external feedback path. The correction signal of the lock box is also applied to the current modulation port of the laser controller via the inverting amplifier to implement a current feedforward.

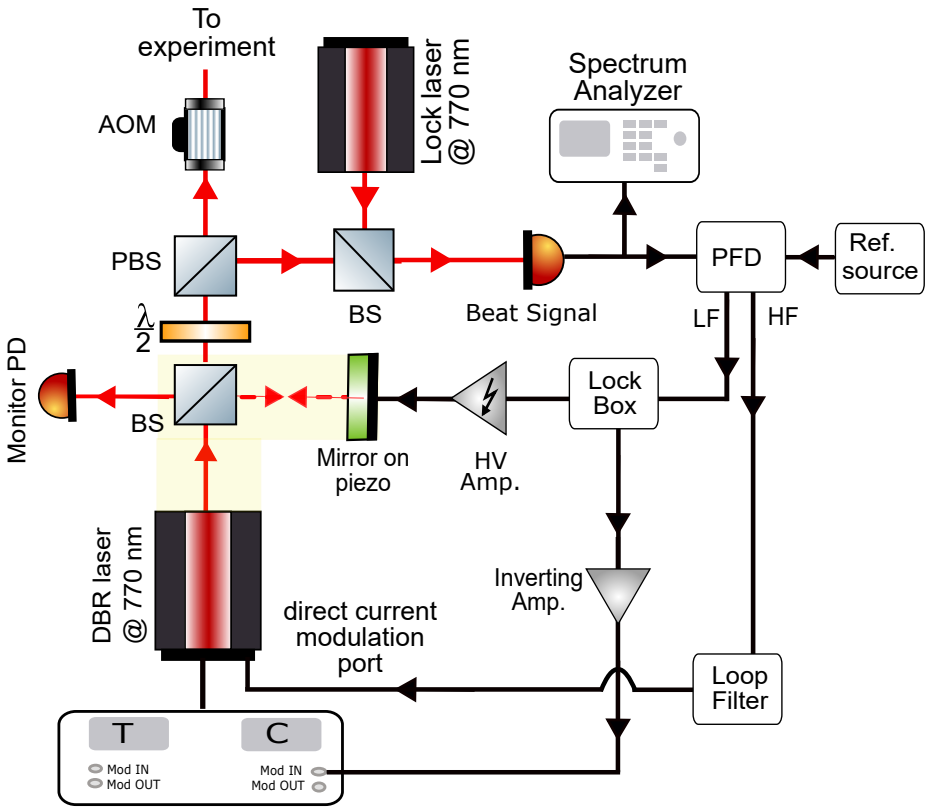

Figure 4.1: Experimental setup for Raman lock between the LR-DBR laser and the lock laser. A phase frequency discriminator (PFD) is used to compare the beat signal of the LR-DBR laser and the lock laser to a stable reference and quantify the frequency and phase deviations. The PFD generates two error signals, a high frequency (HF) output and low frequency output (LF). The HF output is connected to a loop filter, which then applies feedback signal to a direct current modulation on the laser diode for phase locking. The LF output is processed via a PI controller (lock box) to produce a correction signal, which is then amplified via a high voltage (HV) amplifier and applied to the piezo-mirror of the external feedback path. The correction signal of the lock box is also applied to the current modulation port of the laser controller via the inverting amplifier.

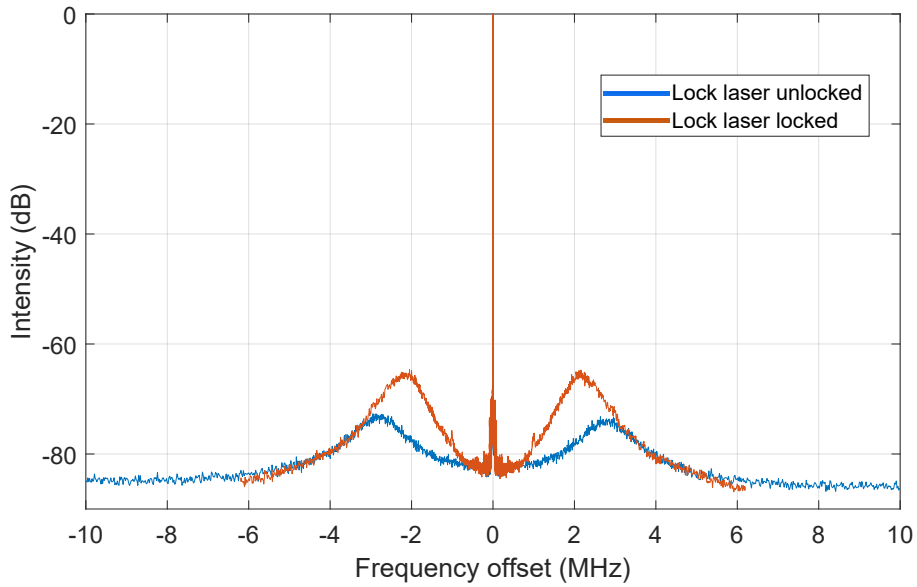

Figure 4.2: Beat spectra of the lock between the LR-DBR laser and the lock laser. The beat spectrum in blue is recorded when the LR-DBR laser is locked to a free-running lock laser with 99.5% power in the carrier and locking bandwidth of ~ 3 MHz. When the Raman laser is locked to the lock laser, and the latter locked to the frequency comb, the phase lock of the Raman amplifies the servo bumps of the lock laser to comb which results in a reduction of the power in the carrier to 97.5% and locking bandwidth to ~2.1 MHz.

The lock laser at 770 nm is also locked to the frequency comb via an OPLL [56, 57]. When the LR-DBR laser is locked to an unlocked (free-running) lock laser the power in the carrier is 99.5% with locking bandwidth (BW) of ~ 3 MHz. However, when the lock laser's lock to the frequency comb is also engaged, the power in the carrier decreases to 97.5% with locking BW of ~2.1 MHz because the phase lock of the Raman can amplify the servo bumps of the lock laser to comb if the bandwidths of these two locks are similar. Beat spectra for two cases are shown in Fig. 4.2.

Lock Box

The lock box comprises of proportional and integral controller which processes the LF error signal to correct for frequency deviations. The output of the lock box is applied to the piezo of the external feedback path via the HV amplifier. Mathematically, it can be written as

$$c(t) = M \cdot [P \cdot e(t) + I \cdot \int_0^t e(\tau) \cdot d\tau] \tag{4.1}$$

where c(t) is correction signal, e(t) is the LF error signal and M, P, I are the coarse, proportional and integral gain. All the three gains can be adjusted from the lock box and are set such that the beat signal has a best signal to noise ratio and bandwidth.

Loop Filter

The loop filter provides negative feedback directly to the current modulation of the DBR laser diode to suppress the phase deviations. It consists of three parts: a low pass filter, a lead filter and a voltage

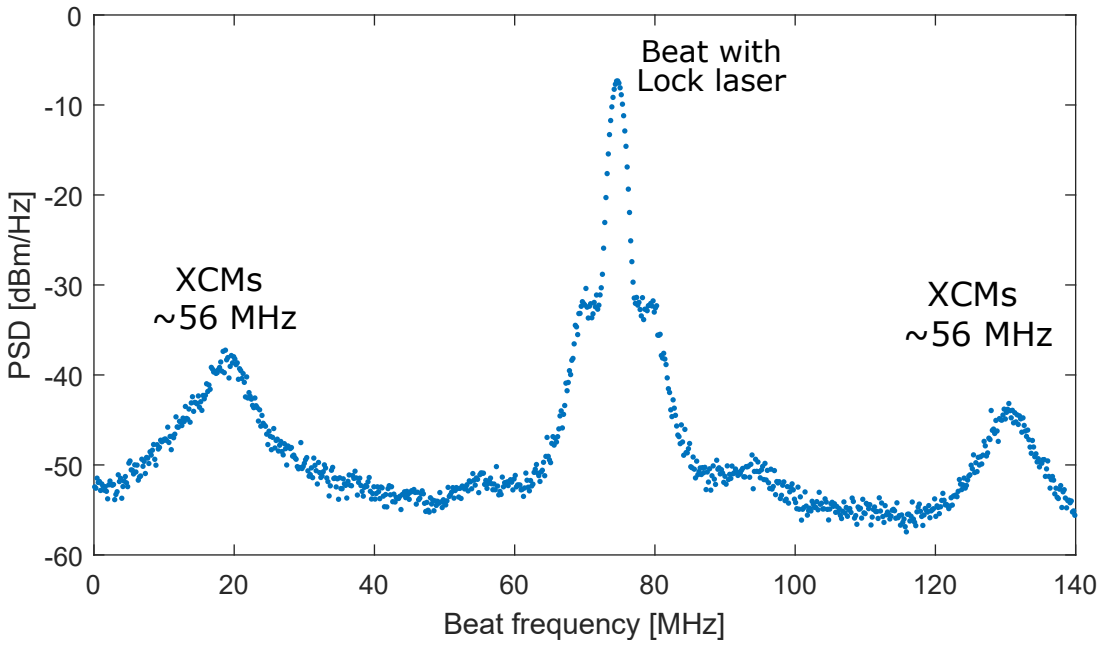

Figure 4.3: Beat spectrum of the LR-DBR laser and the lock laser to reveal the suppressed external cavity modes (XCMs) at ~ 56 MHz from the laser-cavity mode (LCM).

divider. After the low pass filter blocks the frequencies that are high for correction purposes, the lead filter shifts the phase of the signal such that the phase deviations are suppressed. The voltage divider controls the overall gain of the signal. Along with these components are some protection circuitry like the Zener diodes and a DC blocking capacitor at the final output of the loop filter to limit the current feedback sent to the laser diode.

Current Feed-forward

The external optical feedback path (highlighted in yellow in Fig. 4.1) which is 2 m long has free spectral range (FSR) of ~56 MHz and this hampers the frequency tunability of the DBR laser. The external cavity modes (XCMs) present in the vicinity of the laser-cavity mode (LCM) are suppressed by >30 dB but on tuning the frequency of the laser with the piezo the laser jumps between these XCMs. These XCMs are visible in the beat of the LR-DBR laser with the lock laser, see Fig. 4.3. To achieve mode-hop free tuning of frequency over XCMs, a current feedforward was implemented.

The idea was to scan the frequency of the laser with the piezo and the laser current simultaneously such that the laser does not jump between the XCMs, and to do so the output of the lock box was also applied to the current modulation port of the laser controller via the inverting amplifier. The frequency response of the laser with the optical feedback blocked via the current modulation port of the laser controller is -320 MHz/V as compared to 64 MHz/V frequency tuning by the piezo.An inverting amplifier was designed to match the current-tuning slope to the piezo-tuning one, achieving a mode-hop-free tuning range of 1.1 GHz GHz (>20×FSR). Currently, the tuning range is limited by the maximum stroke of the piezo.

4.2 Raman Sideband Cooling

4.2.1 Experimental Setup

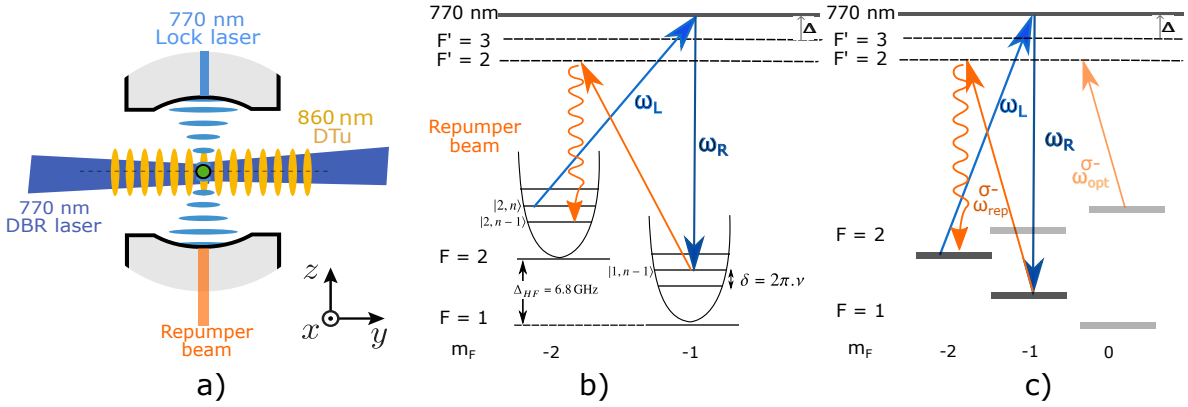

Figure 4.4: (a) A single rubidium atom trapped at the centre of a fiber Fabry-Pérot cavity using a pair of counter-propagating, red-detuned dipole trap beams at 860 nm in the xy plane (the 860 nm beam in x-axis is not shown) and the intra-cavity, blue-detuned laser field at 770 nm in z-axis. Circularly polarized light at 795 nm to optically pump the atom. The LR-DBR laser beam propagates collinear to the DT_u in y-axis (b) Illustration of 1-D Raman sideband cooling using the lock laser (ω_L) and the Raman laser (ω_R). (c) Details of the levels and transitions in ^{87}Rb involved in Raman manipulation and cooling. The figure is adapted from [2].

In our experiment, a neutral ^{87}Rb atom is loaded at the centre of a fiber Fabry-Pérot cavity [1, 2]. Inside the cavity, the atom is confined in the xy plane using a pair of counter-propagating, red-detuned dipole trap beams at 860 nm (referred to as DT_v and DT_u). The vertical confinement is provided by the intra-cavity, blue-detuned laser field at 770 nm, it is also used to stabilize the cavity length via the Pound-Drever-Hall method [58]. The quantization axis in the experiment is defined by magnetic bias field bias of ~1.82 G along the cavity axis (z-axis). This field breaks the degeneracy of the hyperfine energy levels with the Zeeman splitting $\Delta\omega_B = 2\pi.1.27$ MHz.

In order to achieve coherent two-photon coulping between the $F = 2$ and the $F = 1$ manifold (strictly speaking $|F = 2, m_F = -2\rangle$ and $|F = 1, m_F = -1\rangle$) (Fig. 4.4(b)) of the $5^2S_{1/2}$ electronic ground state hyperfine, we address the atom by a single Raman laser beam that propagates collinear to the DT_u along the y-axis. This Raman beam is the LR-DBR laser that is phase-locked to the intra-cavity, blue-detuned laser field (referred as lock laser) with a tunable frequency offset $\Delta_{HF} = 6.8$ GHz plus a variable two-photon detuning $\delta = 2\pi.\nu$.

The blue detuned standing-wave intra-cavity dipole trap created by lock laser light serves as second Raman field, eliminating the need of an additional Raman beam. Since the atoms are trapped at the intensity minima of the intra cavity lattice, two-photon carrier Raman transitions are suppressed [4, 5]. With this configuration of the Raman beams, we expect to cool the atom in both z and y direction.

In our experiment, the red detuned horizontal dipole traps at 860 nm are not exactly orthogonal to each other and this finite non-orthogonality leads to small projection of the Raman beam onto DT_v (x-axis), enabling Raman transitions in this direction also. Note: From now on, the term "Raman laser" and "LR-DBR laser" will be used interchangeably.

4.2.2 Motional State Coupling

To understand the suppression of the carrier transition, we look at how the Raman laser beams couple to the motional states of the trapped atom. The atoms are trapped at the node of the standing wave along the z-axis which also serves as one of the Raman arms, therefore, the electric field amplitude is proportional to $\sin\left(\vec{k}_z\hat{z}\right)$. The resonant coupling between the spin-motional states is described by [4, 5]

$$\Omega_{\uparrow m_y m_z,\downarrow m_y' m_z'} = \Omega_o \left|\left\langle \uparrow m_y' m_z' \right| \sin\left(\vec{k}_z\hat{z}\right) \exp\left(i\vec{k}_y\hat{y}\right)\hat{\sigma}^\dagger \left|\downarrow m_y m_z\right\rangle\right| \tag{4.2}$$

where m_y, m_z, m_y', m_z' denote the motional quantum numbers of the initial and the final state, $\hat{y}$ and $\hat{z}$ are the position operators. $\vec{k}_y$ and $\vec{k}_z$ are the wave vectors of the two Raman fields. $\hat{\sigma}^\dagger$ is the spin raising operator and the $\Omega_o \sim 400\,\mathrm{kHz}$ is theoretically calculated bare two-photon Rabi frequency which depends on the laser powers, detuning and the internal states.

In the Lamb-Dicke regime [59], the geometry of the light fields in Eq. 4.2 can be re-written in the first-order terms of harmonic oscillator raising $\hat{a}_z^\dagger$, $\hat{a}_y^\dagger$ and lowering operators $\hat{a}_z$, $\hat{a}_y$ as

$$\begin{aligned}\sin\left(\vec{k}_z\hat{z}\right)\exp\left(i\vec{k}_y\hat{y}\right) &\approx (\vec{k}_z\hat{z})(\mathbb{1} + i\vec{k}_y\hat{y}) \\ &= \eta_z(\hat{a}_z^\dagger + \hat{a}_z) + i\eta_y\eta_z(\hat{a}_z^\dagger\hat{a}_y^\dagger + \hat{a}_z\hat{a}_y^\dagger + \hat{a}_z^\dagger\hat{a}_y + \hat{a}_z\hat{a}_y)\end{aligned} \tag{4.3}$$

$\eta_z = 0.13$ and $\eta_y = 0.13$ are the Lamb-Dicke parametrs along the y- and the z-axis. The equation above imposes the selection rule $\Delta m_z = \pm 1, \pm 3$ for the standing wave Raman field in z-axis, and the carrier transitions are suppressed. The first order cooling and heating sideband along z-axis scale with $\Omega_o\eta_z$. The motion along y- and z-axis couple with scaling factor $\Omega_o\eta_z\eta_y$.

As already mentioned, the Raman beam send along y-axis is not perpendicular to the DT_v. This misalignment modifies the Lamb-Dicke parameters to $\eta_z = 0.11$ and $\eta_y = 0.14$ and gives rise to a finite Lamb-Dicke parameter in x-axis $\eta_x = 0.017$.

Carrier Suppression

The blue-detuned Lock laser confines atom in the z-axis close to the minimum of the light intensity. According to Eq. 4.3, full carrier suppression is expected if the atom is confined perfectly at the minimum of the light intensity of the blue-detuned Lock laser. However, that may not be the case. For example intensity imbalance of the two beams forming the optical standing wave, external forces displacing the trap centre from intensity minimum, residual gravitational sag [4] could lead to residual carrier Raman coupling. Observation of limited carrier transitions due to running-wave component of the cavity field has already been reported for our system in the past [2].

4.2.3 Cooling Scheme

In order to understand the cooling scheme one can consider the ^{87}Rb atom as a three level atom consisting of two metastable ($|1\rangle$ and $|2\rangle$) state and an excited state $|3\rangle$. The state $|1\rangle$ and $|2\rangle$ correspond to $\left|F = 2, m_F = -2\right\rangle$ and $\left|F = 1, m_F = -1\right\rangle$) of the $5^2S_{1/2}$ electronic hyperfine ground state, respectively. $|3\rangle$ is a virtual state. The cooling scheme is shown in (Fig. 4.4(b)). The lock laser sets the single-photon detuning $\Delta = 2\pi \times 4.8\,\mathrm{THz}$, while the two-photon detuning δ between the Raman beams is given by the trap frequency ν.

The first step is a stimulated Raman transition which couples to the motional state of the atom as well as the internal. The atom starts in state $|2, n\rangle$, where n is the vibrational level (Fig. 4.4(b)). It is then pumped to the virtual intermediate state $|3\rangle$ by the lock laser. After the stimulated emission of a second photon into the LR-DBR beam, the atom decays to state $|1, n-1\rangle$ if the the two-photon detuning $\delta = +2\pi.\nu$, thereby loosing a motional quanta and cooling the atom. The atom is then pumped to $\left|F' = 2, m_F = -2\right\rangle$ using σ^- polarized optical pumper and repumper (Fig. 4.4(c)). In the Lamb-Dicke regime $\eta_i \ll 1$ (i = x, y, z), the atom will spontaneously decay into $|2, n-1\rangle$. After sufficient iterations of this process, the atom reaches the motional ground state $|2, 0\rangle$, which is dark with respect to both pumping and Raman beams.

In our experiment, the atom is confined in 3D with the trap frequencies, ν_x, ν_y, ν_z. We wish to cool the atom in 3D motional ground state using a single Raman pulse. In order to achieve this, we overlap the trap frequencies of the three dipole traps and drive the cooling transition at the overlapped frequency ν_{ov}. With the aim of calibrating and later overlapping the trap frequencies of all three optical lattices, we perform Raman spectroscopy.

4.3 Raman Spectroscopy and Cooling

The axial oscillation frequency of an atom in a standing wave dipole trap dipole trap created by a pair of counter-propagating laser beams of wavelength λ can be written using the harmonic approximation as [60]

$$\omega_{axial} = 2\pi \cdot \sqrt{\frac{2U_o}{m\lambda^2}} \tag{4.4}$$

where m is the mass of ^{87}Rb and U_o is the depth of the trapping potential. Power of the interfering pair of beams that create the standing wave varies linearly with the power P of the dipole trap beam, the trap frequency should follow a dependence $\omega_{axial} \sim \sqrt{P}$. For such calibration, we recorded Raman spectra for different dipole trap depths.

4.3.1 Experimental Sequence for Raman Spectroscopy

The experimental sequence of the Raman spectroscpoy starts after a successful single atom loading event at the centre of the cavity. The measurement sequence initializes the atom with high fidelity in the $\left|F = 2, m_F = -2\right\rangle$ by a 100 µs optical pumping pulse. The optical pumping pulse consists of repumper (ω_{rep}) and optical pump light (ω_{opt}), both σ^- polarized and resonant with the $F = 2 \rightarrow F' = 2$ and $F = 1 \rightarrow F' = 2$ D1 transition (Fig. 4.4(c)). A single Raman pulse of 500 ms of 1.25 mW focused to 11 µm beam waist is applied to the atoms, followed by 3 ms state detection. The presence of the atom in $F = 2$ is detected with help of the cavity aided non-destructive detection of the atom distinguishing between cavity coupled $F = 2$ and uncoupled $F = 1$ state [2]. The details of the steps before the Raman spectroscopy which includes transporting and loading the atom in the cavity and cooling the atoms with degenerate Raman sideband cooling can be found in [1, 2, 7].

In order to recycle the same atom for multiple experimental repetitions, the atom is cooled using the Raman sideband cooling before the Raman spectroscopy sequence. The Raman laser, the repumper and the optical pump light are turned on for 1 ms. We address the cooling sideband by setting the two-photon detuning $\delta/2\pi$ to 90 kHz, blue-detuned with respect to the carrier transition (Note: This cooling frequency was found experimentally by trying different frequencies). This enables us to recycle the atom upto 200

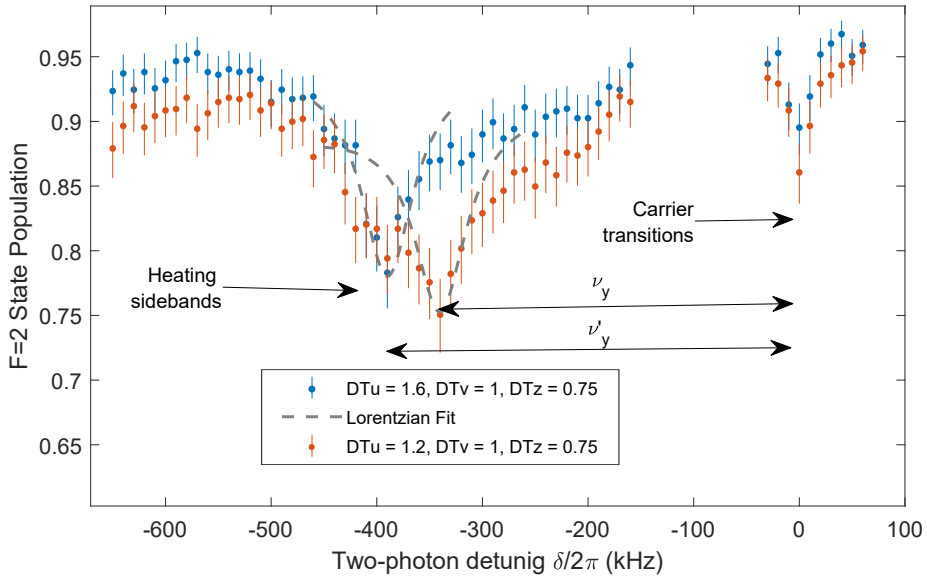

Figure 4.5: Raman spectrum recorded by tuning the two-photon detuning δ for two different powers of DT_u, the atom is cooled using Raman sideband cooling before the Raman spectroscopy to increase the recycling rate of the atom. The suppressed carrier transition is visible at a two-photon detuning $\delta = 0$ MHz. To the left of the carrier are the heating sidebands. The peak at ν_y =344.2 kHz moved to ν'_y =400.1 kHz when the power in DT_u is increased by 60%. The power of each dipole trap is given in relative units. Relative to the usual operation condition summarised in Table. 4.1.

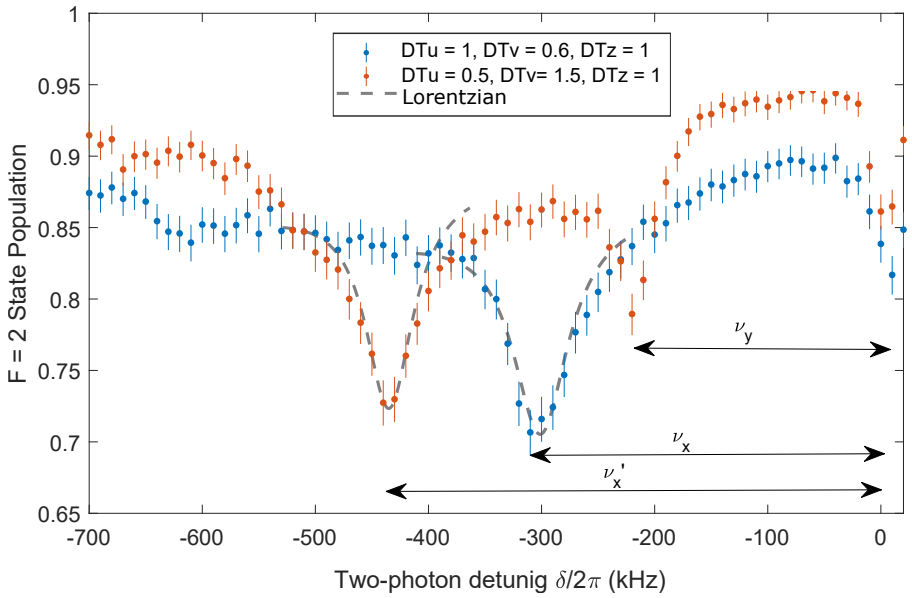

Figure 4.6: Raman spectrum recorded by tuning the two-photon detuning δ, the atom is cooled using Raman sideband cooling before the Raman spectroscopy to increase the recycling rate of the atom. At two-photon detuning $\delta = 0$ is the suppressed carrier transition. To the left of the carrier are the heating sidebands. The peak at ν_x =316.4 kHz moved to ν'_x =439.5 kHz when the power in DT_v is increased by 90%. The power of each dipole trap is given in relative units. Relative to the usual operation condition summarised in Table. 4.1.

Dipole Trap	Power (mW)	Beam waist (μm)
DT_u	84.4	13
DT_v	83.9	11
DT_z	1.8	5

Table 4.1: Usual operation condition for the dipole traps. All the powers are relative to these values.

times, during which the two-photon detuning is scanned. Every sequence has a 100 ms atom presence check which enables to post-select the data upon the survival of the atom.

To characterise the trap frequency in y-axis corresponding to DT_u, the power of the DT_v and DT_z was fixed while scanning the power of DT_u. Note: All the power mentioned are relative to power summarised in Table. 4.1, where $DT_u = 1$ is the usual operation condition with power corresponding to 84.4 mW. So, $DT_u = 1.2$ indicates an increase by 20% from the $DT_u = 1$ condition. The Raman spectrum for two different powers of DT_u are shown in Fig. 4.5. The peak at the zero is the suppressed carrier, on the left of the carrier are the heating sidebands. The peak at 341 kHz moved to 392.5 kHz when the power was increased by 60%. The recorded spectra are fitted with Lorentzian curves to find the position of the peak. Similarly, the sideband corresponding to DT_v was identified by changing the power of DT_v and DT_u simultaneously (Fig. 4.6). Note: $DT_v = 1$ corresponds to 83.9 mW.

To identify the position of the z-sideband corresponding to DT_z, we scanned the power of DT_z by turning DT_u off as soon as an atom is successfully transported to the cavity region while keeping DT_v fixed. Only first order sidebands of the motion along the z-axis are expected. Inhomogeneous effects due to the distribution of atom positions in the 3D trap broadens the spectrum (Fig. 4.7). This effect is the most prominent in z-direction because the beam waist of the DT_z (~5 µm) is approximately half of the beam waist of the DT_u (~13 µm) and DT_v (~11 µm).

Fig. 4.8 summarises the power dependence of the trap frequencies acquired with multiple measurements as the ones shown above. Measured data for each dipole trap is fitted with a function

$$\nu = \nu_o + a \times \sqrt{P} \tag{4.5}$$

The resulting fit parameters and the respective confidence intervals (CI) are presented in the table below

	a [kHz/$\sqrt{\text{mW}}$][CI]	ν_o [kHz][CI]
DTu	312 [283, 340]	0 [-27, 27]
DTv	295.16 [93.0, 497.2]	89.9 [-119.5, 299.4]
DTz	426.4 [322.9, 530.0]	-243.1 [-392.9, -93.3]

The offset in the trapping frequency could be attributed to incorrect calibration of power or possible light shifs. Few fitting points available in the low power region could be responsible for the poor CI on the fitting parameters for DT_v. The trap frequency of DT_z has a significant offset this could be attributed to the inhomogeneous broadening or light shifts introduced by the D1 beams. We wish to characterise the trap frequency of DT_z again using parametric heating [61, 62].

With the calibration of the trap frequencies for DT_u and DT_v and a rough estimate of the trap frequency of DT_z, we overlapped all the sidebands at ~ 370 kHz. Fig. 4.9 shows one final spectrum with overlapped sidebands. The suppressed cooling sideband on the right side of the carrier indicates near 3D motional ground state cooling.

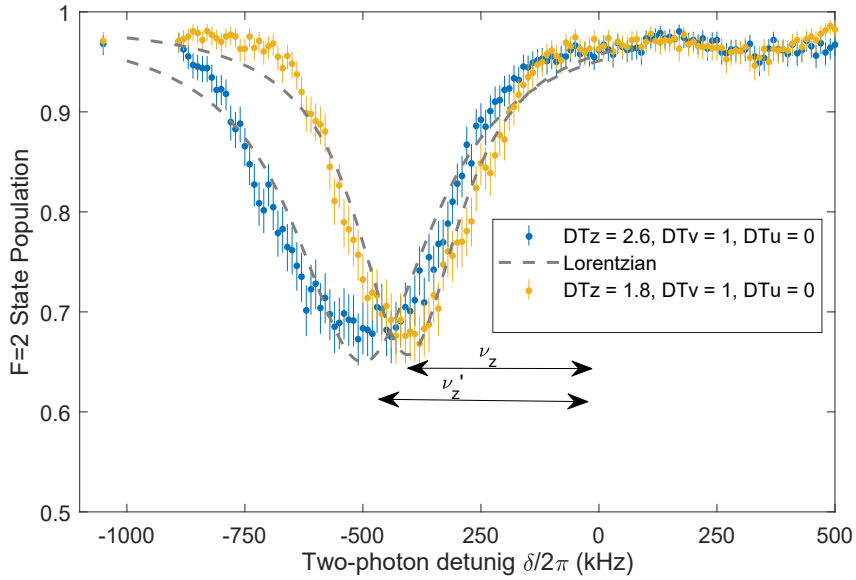

Figure 4.7: Inhomogeneously broadened spectrum corresponding to DTz when DTu is adiabatically lowered to zero. The power of each dipole trap is given in units relative to the usual operation condition summarised in Table. 4.1. The trap frequency changed from ν_z=370.5 kHz to ν_z'=436.3 kHz.

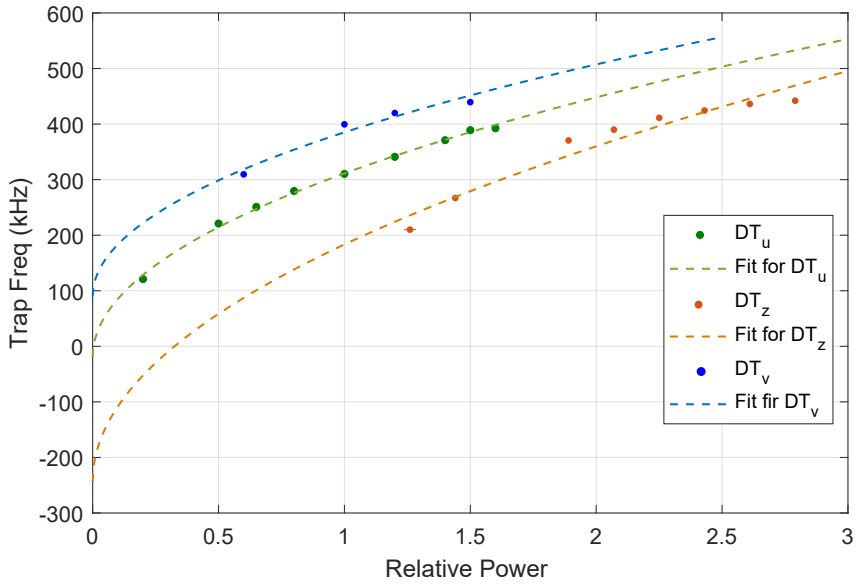

Figure 4.8: Square root dependence of trap frequency on laser power (units relative to value given in Table. 4.1) for the three dipole traps. Each data point is determined by fitting a Lorentzian peak to experimentally obtained Raman spectrum, the error on the positon of peak was found to be too small to be visible on the scale of the y-axis here.

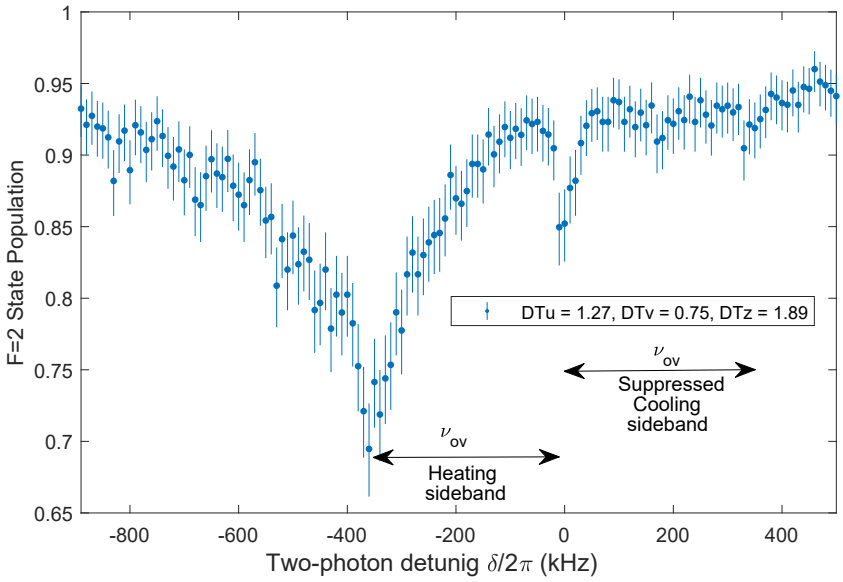

Figure 4.9: Three trap frequencies overlapped at $\sim 370\,\text{kHz}$. Due to the presence of three trapping frequencies, and their corresponding sidebands, the temperature of the cold atoms cannot be determined using the models presented in [2, 4]. However, the height of the cooling sidebands on the right of the carrier indicate near 3D motional ground state cooling.

4.4 Conclusion

The Raman laser system implemented with the LR-DBR laser fulfils one of the most important criteria of being stable and robust over longer time periods which marks a huge technical improvement for the experiment in general. With preliminary characterization of the trap frequency corresponding to the three dipole traps in our experimental setup, we overlapped them at $\sim 370\,\text{kHz}$. The larger aim of being able to cool in all the three directions with a single Raman pulse is already midway, evident from the height to the cooling sidebands on the right side of the carrier in the final spectrum Fig. 4.9. The fine optimisation of the Raman laser power, Raman pulse length and repumping time is under progress. The lifetime of the atom in the cavity under continuous cooling and without any other interaction is as long as $\sim 1\,\text{min}$, allowing to recycle the same atom for 30000 experimental attempts. Once the cooling is optimised, we wish to image the single atom inside the cavity via the light scattered during continuous Raman sideband cooling, using a technique called Raman cooling imaging [63].

CHAPTER 5

Conclusion

In this thesis, I have presented an external optical feedback scheme to reduce the Lorentzian linewidth of the distributed Bragg reflector laser (DBR) laser. To characterise the effect of the optical feedback on the linewidth of the DBR laser, a delayed-self heterodyne (DSH) measurement was set up. As estimated later using the simulation-based fitting routine, the optical feedback reduced the Lorentzian linewidth from 736.8 kHz to 0.5 kHz, when the feedback power ratio p was −38.8 dB. Based on [24], we developed and extended the simulation-based fitting routine to extract various linewidth components from the DSH spectrum. The advantage of this fitting is that it can be used for both uncorrelated- and correlated-type DSH spectra. Not only did we predict the Lorentzian linewidth using three different methods, but we can also estimate the linewidth component arising from the higher order frequency noise. For the operation of the experiment we chose a feedback power ratio of approximately −44.4 dB.

The second part of my thesis focussed on implementing carrier-free Raman sideband cooling as a tool for future atom-cavity experiments. This cooling technique requires the Raman laser being phase locked to the already existing cavity lock laser, that also generates the blue detuned intra-cavity lattice along the z-axis, without need of an additional Raman beam in the experimental setup. To achieve near ground state cooling of the atom with a single Raman pulse, we characterised and overlapped the three trap frequencies at ∼370 kHz. However, we wish to characterise the intra cavity trap frequency ν_z again using parametric heating [61, 62]. Due to the presence of three trapping frequencies, and their corresponding sidebands, the temperature of the cold atoms cannot be determined using the models presented in [2, 4]. Therefore, as a qualitative figure of merit of the cooling efficiency, we measure the lifetime and the recycling rate of the atom. The repeated cooling cycles of a given time interval, enhances the lifetime of the atoms in a 3D lattice to around ∼ 1 min as compared to ∼ 700 ms in the dark (meaning only the lattice beams are on). Per single atom ∼ 30, 000 photon storage attempts are possible, which is almost thrice the value we had earlier. The lock is robust and stable for at least 3 days, increasing the duty cycle of the experiment and allowing for reliable measurements during the nights and over the weekend from home.

After optimising the Raman sideband cooling, we plan to image single atom inside of the cavity via Raman cooling imaging [63]. Detecting the resonant repumper photons involved in the Raman cooling process itself, allows for the non-destructive and long exposure images of the atoms.

References

[1] J. C. Gallego. “Strong Coupling between Small Atomic Ensembles and an Open Fiber Cavity”. PhD thesis. 2017 (cit. on pp. 3, 39, 41).

[2] T. Macha. “ Storage of Short Light Pulses in a Fiber–Based Atom–Cavity System”. PhD thesis. 2018 (cit. on pp. 3, 4, 35, 39–41, 45, 47).

[3] T. Macha et al. *Non-adiabatic Storage of Short Light Pulses in an Atom-Cavity System*. 2019. arXiv: 1903.10922 [physics.atom-ph] (cit. on p. 3).

[4] R. Reimann. “Cooling and Cooperative Coupling of Single Atoms in an Optical Cavity”. PhD thesis. 2014 (cit. on pp. 3, 4, 35, 39, 40, 45, 47).

[5] R. Reimann et al. “Carrier-free Raman manipulation of trapped neutral atoms”. In: *New Journal of Physics* 16.11 (Nov. 2014), p. 113042. DOI: 10.1088/1367-2630/16/11/113042 (cit. on pp. 3, 35, 39, 40).

[6] V. Vuleti ć et al. “Degenerate Raman Sideband Cooling of Trapped Cesium Atoms at Very High Atomic Densities”. In: *Phys. Rev. Lett.* 81 (26 Dec. 1998), pp. 5768–5771. DOI: 10.1103/PhysRevLett.81.5768. URL: https://link.aps.org/doi/10.1103/PhysRevLett.81.5768 (cit. on p. 3).

[7] E. Uruñuela et al. “Ground-state cooling of a single atom inside a high-bandwidth cavity”. In: *Phys. Rev. A* 101 (2 Feb. 2020), p. 023415. DOI: 10.1103/PhysRevA.101.023415. URL: https://link.aps.org/doi/10.1103/PhysRevA.101.023415 (cit. on pp. 3, 41).

[8] M. E. Gehm et al. “Dynamics of noise-induced heating in atom traps”. In: *Phys. Rev. A* 58 (5 Nov. 1998), pp. 3914–3921. DOI: 10.1103/PhysRevA.58.3914. URL: https://link.aps.org/doi/10.1103/PhysRevA.58.3914 (cit. on p. 3).

[9] T. A. Savard, K. M. O’Hara and J. E. Thomas. “Laser-noise-induced heating in far-off resonance optical traps”. In: *Phys. Rev. A* 56 (2 Aug. 1997), R1095–R1098. DOI: 10.1103/PhysRevA.56.R1095. URL: https://link.aps.org/doi/10.1103/PhysRevA.56.R1095 (cit. on p. 3).

[10] X. Baillard et al. “Interference-filter-stabilized external-cavity diode lasers”. In: *Optics Communications* 266.2 (2006), pp. 609–613. ISSN: 0030-4018. DOI: https://doi.org/10.1016/j.optcom.2006.05.011. URL: http://www.sciencedirect.com/science/article/pii/S0030401806004561 (cit. on p. 3).

[11] A. L. Schawlow and C. H. Townes. “Infrared and Optical Masers”. In: *Phys. Rev.* 112 (6 1958), pp. 1940–1949. DOI: 10.1103/PhysRev.112.1940. URL: https://link.aps.org/doi/10.1103/PhysRev.112.1940 (cit. on pp. 3, 5, 9, 21, 32).

[12] C. Henry. “Theory of the linewidth of semiconductor lasers”. In: *IEEE Journal of Quantum Electronics* 18.2 (1982), pp. 259–264. DOI: 10.1109/JQE.1982.1071522 (cit. on pp. 3, 5, 7, 9, 21, 32).

[13] T. Kanada and K. Nawata. “Injection laser characteristics due to reflected optical power”. In: *IEEE Journal of Quantum Electronics* 15.7 (July 1979), pp. 559–565. ISSN: 1558-1713. DOI: 10.1109/JQE.1979.1070065 (cit. on pp. 3, 5).

[14] R. Lang and K. Kobayashi.
"External optical feedback effects on semiconductor injection laser properties".
In: *IEEE Journal of Quantum Electronics* 16.3 (Mar. 1980), pp. 347–355. ISSN: 1558-1713.
DOI: 10.1109/JQE.1980.1070479 (cit. on pp. 3, 5, 7).

[15] G. Agrawal. "Line narrowing in a single-mode injection laser due to external optical feedback".
In: *IEEE Journal of Quantum Electronics* 20.5 (1984), pp. 468–471. ISSN: 1558-1713.
DOI: 10.1109/JQE.1984.1072420 (cit. on pp. 3, 5, 9).

[16] L. Goldberg et al. "Spectral Characteristics of Semiconductor Lasers with Optical Feedback".
In: *IEEE Transactions on Microwave Theory and Techniques* 30.4 (1982), pp. 401–410.
ISSN: 1557-9670. DOI: 10.1109/TMTT.1982.1131081 (cit. on pp. 3, 5).

[17] S. Saito and Y. Yamamoto. "Direct observation of Lorentzian lineshape of semiconductor laser and linewidth reduction with external grating feedback".
In: *Electronics Letters* 17.9 (Apr. 1981), pp. 325–327. ISSN: 0013-5194.
DOI: 10.1049/el:19810229 (cit. on pp. 3, 5).

[18] Q. Lin et al.
"Long-external-cavity distributed Bragg reflector laser with subkilohertz intrinsic linewidth".
In: *Opt. Lett.* 37.11 (June 2012), pp. 1989–1991. DOI: 10.1364/OL.37.001989.
URL: http://ol.osa.org/abstract.cfm?URI=ol-37-11-1989 (cit. on pp. 3, 12).

[19] R. Tkach and A. Chraplyvy. "Regimes of feedback effects in 1.5-μm distributed feedback lasers".
In: *Journal of Lightwave Technology* 4.11 (Nov. 1986), pp. 1655–1661.
DOI: 10.1109/JLT.1986.1074666 (cit. on pp. 3, 5, 9, 11).

[20] T. Okoshi, K. Kikuchi and A. Nakayama.
"Novel method for high resolution measurement of laser output spectrum".
In: *Electronics Letters* 16.16 (July 1980), pp. 630–631. DOI: 10.1049/el:19800437
(cit. on pp. 4, 15).

[21] Y. Kotaki and H. Ishikawa.
"Spectral characteristics of a three-section wavelength-tunable DBR laser".
In: *IEEE Journal of Quantum Electronics* 25.6 (1989), pp. 1340–1345 (cit. on pp. 4, 15, 22).

[22] T. N. Huynh, L. Nguyen and L. P. Barry. "Phase Noise Characterization of SGDBR Lasers Using Phase Modulation Detection Method With Delayed Self-Heterodyne Measurements".
In: *J. Lightwave Technol.* 31.8 (Apr. 2013), pp. 1300–1308.
URL: http://jlt.osa.org/abstract.cfm?URI=jlt-31-8-1300 (cit. on pp. 4, 15, 22).

[23] M.-C. Amann et al. "Linewidth broadening by 1/f noise in wavelength-tunable laser diodes".
In: *Applied Physics Letters* 70.12 (1997), pp. 1512–1514. DOI: 10.1063/1.118603.
eprint: https://doi.org/10.1063/1.118603.
URL: https://doi.org/10.1063/1.118603 (cit. on pp. 4, 15, 22).

[24] W. Ma et al.
"Laser frequency noise characterization by self-heterodyne with both long and short delay".
In: *Appl. Opt.* 58.13 (May 2019), pp. 3555–3563. DOI: 10.1364/AO.58.003555.
URL: http://ao.osa.org/abstract.cfm?URI=ao-58-13-3555
(cit. on pp. 4, 15, 20, 22–24, 47).

[25] Y. Tohmori and M. Oishi. “1.55 ¯ m Butt-Jointed Distributed Bragg Reflector Lasers Grown Entirely by Low-Pressure MOVPE”.
In: *Japanese Journal of Applied Physics* 27.Part 2, No. 4 (Apr. 1988), pp. L693–L695.
DOI: 10.1143/jjap.27.l693 (cit. on p. 5).

[26] M.-C. Amann. “Chapter 3 - Single-Mode and Tunable Laser Diodes”. In: *Semiconductor Lasers II*. Ed. by E. Kapon. Optics and Photonics. San Diego: Academic Press, 1999, pp. 157–258.
DOI: https://doi.org/10.1016/B978-012397631-4/50003-3.
URL: http://www.sciencedirect.com/science/article/pii/B9780123976314500033 (cit. on p. 5).

[27] K. Kikuchi and T. Okoshi. “Simple formula giving spectrum-narrowing ratio of semiconductor-laser output obtained by optical feedback”. English.
In: *Electronics Letters* 18 (1 Jan. 1982), 10–12(2). ISSN: 0013-5194. URL: https://digital-library.theiet.org/content/journals/10.1049/el_19820008 (cit. on p. 5).

[28] G. P. Agrawal and N. K. Dutta. *Distributed-Feedback Semiconductor Lasers*.
Boston, MA: Springer US, 1993, pp. 319–384. ISBN: 978-1-4613-0481-4.
DOI: 10.1007/978-1-4613-0481-4_7.
URL: https://doi.org/10.1007/978-1-4613-0481-4_7 (cit. on pp. 5, 6).

[29] R. G. Hunsperger. “Distributed Feedback Lasers”. In: *Integrated Optics: Theory and Technology*. Berlin, Heidelberg: Springer Berlin Heidelberg, 1991, pp. 220–235. ISBN: 978-3-540-48730-2.
DOI: 10.1007/978-3-540-48730-2_13.
URL: https://doi.org/10.1007/978-3-540-48730-2_13 (cit. on p. 6).

[30] A. Olsson and C. Tang.
“Coherent optical interference effects in external-cavity semiconductor lasers”.
In: *IEEE Journal of Quantum Electronics* 17.8 (Aug. 1981), pp. 1320–1323. ISSN: 1558-1713.
DOI: 10.1109/JQE.1981.1071272 (cit. on p. 7).

[31] G. P. Agrawal and N. K. Dutta. “Rate Equations and Operating Characteristics”. In: *Semiconductor Lasers*. Boston, MA: Springer US, 1993, pp. 231–318. ISBN: 978-1-4613-0481-4.
DOI: 10.1007/978-1-4613-0481-4_6.
URL: https://doi.org/10.1007/978-1-4613-0481-4_6 (cit. on p. 8).

[32] C. Henry. “Phase noise in semiconductor lasers”.
In: *Journal of Lightwave Technology* 4.3 (Mar. 1986), pp. 298–311. ISSN: 1558-2213.
DOI: 10.1109/JLT.1986.1074721 (cit. on p. 9).

[33] C. Henry. “Theory of the linewidth of semiconductor lasers”.
In: *IEEE Journal of Quantum Electronics* 18.2 (1982), pp. 259–264.
DOI: 10.1109/JQE.1982.1071522 (cit. on p. 9).

[34] D. Lenstra, B. Verbeek and A. Den Boef.
“Coherence collapse in single-mode semiconductor lasers due to optical feedback”.
In: *IEEE Journal of Quantum Electronics* 21.6 (June 1985), pp. 674–679. ISSN: 1558-1713.
DOI: 10.1109/JQE.1985.1072725 (cit. on p. 12).

[35] S. Camatel and V. Ferrero. “Narrow Linewidth CW Laser Phase Noise Characterization Methods for Coherent Transmission System Applications”.
In: *Journal of Lightwave Technology* 26.17 (2008), pp. 3048–3055 (cit. on p. 15).

[36] M. Schiemangk et al. “Accurate frequency noise measurement of free-running lasers”. In: *Appl. Opt.* 53.30 (Oct. 2014), pp. 7138–7143. DOI: 10.1364/AO.53.007138. URL: http://ao.osa.org/abstract.cfm?URI=ao-53-30-7138 (cit. on p. 15).

[37] M. Kourogi and M. Ohtsu. “Novel optical frequency discriminator for FM noise reduction of semiconductor lasers”. In: *Optics Communications* 81.3 (1991), pp. 204–208. ISSN: 0030-4018. DOI: https://doi.org/10.1016/0030-4018(91)90639-U. URL: http://www.sciencedirect.com/science/article/pii/003040189190639U (cit. on p. 15).

[38] S. Camatel and V. Ferrero. “Narrow Linewidth CW Laser Phase Noise Characterization Methods for Coherent Transmission System Applications”. In: *J. Lightwave Technol.* 26.17 (Sept. 2008), pp. 3048–3055. URL: http://jlt.osa.org/abstract.cfm?URI=jlt-26-17-3048 (cit. on p. 15).

[39] P. Gallion and G. Debarge. “Quantum phase noise and field correlation in single frequency semiconductor laser systems”. In: *IEEE Journal of Quantum Electronics* 20.4 (Apr. 1984), pp. 343–349. DOI: 10.1109/JQE.1984.1072399 (cit. on pp. 15, 16).

[40] L. Richter et al. “Linewidth determination from self-heterodyne measurements with subcoherence delay times”. In: *IEEE Journal of Quantum Electronics* 22.11 (1986), pp. 2070–2074 (cit. on p. 17).

[41] C. Greiner et al. “Laser frequency stabilization by means of optical self-heterodyne beat-frequency control”. In: *Opt. Lett.* 23.16 (Aug. 1998), pp. 1280–1282. DOI: 10.1364/OL.23.001280. URL: http://ol.osa.org/abstract.cfm?URI=ol-23-16-1280 (cit. on pp. 17, 19).

[42] R. Ulrich and A. Simon. “Polarization optics of twisted single-mode fibers”. In: *Appl. Opt.* 18.13 (July 1979), pp. 2241–2251. DOI: 10.1364/AO.18.002241. URL: http://ao.osa.org/abstract.cfm?URI=ao-18-13-2241 (cit. on p. 18).

[43] U. Schünemann et al. “Simple scheme for tunable frequency offset locking of two lasers”. In: *Review of Scientific Instruments* 70.1 (1999), pp. 242–243. DOI: 10.1063/1.1149573. eprint: https://doi.org/10.1063/1.1149573. URL: https://doi.org/10.1063/1.1149573 (cit. on p. 19).

[44] L. B. Mercer. “1/f frequency noise effects on self-heterodyne linewidth measurements”. In: *Journal of Lightwave Technology* 9.4 (Apr. 1991), pp. 485–493. DOI: 10.1109/50.76663 (cit. on pp. 19, 20, 22, 31, 32).

[45] H. E. Rowe. Princeton, N.J., Van Nostrand, 1965 (cit. on p. 19).

[46] R. Hakimi and M.-C. Amann. “Reduction of 1/f carrier noise in InGaAsP/InP heterostructures by sulphur passivation of facets”. In: *Semiconductor Science and Technology* 12.7 (July 1997), pp. 778–780. DOI: 10.1088/0268-1242/12/7/004 (cit. on p. 22).

[47] M. Fukuda et al. “1/f noise behavior in semiconductor laser degradation”. In: *IEEE Photonics Technology Letters* 5.10 (1993), pp. 1165–1167 (cit. on p. 22).

[48] K. Kikuchi.
"Effect of 1/f-type FM noise on semiconductor-laser linewidth residual in high-power limit".
In: *IEEE Journal of Quantum Electronics* 25.4 (1989), pp. 684–688 (cit. on p. 22).

[49] P. Welch. "The use of fast Fourier transform for the estimation of power spectra: A method based on time averaging over short, modified periodograms".
In: *IEEE Transactions on Audio and Electroacoustics* 15.2 (1967), pp. 70–73 (cit. on pp. 24, 25).

[50] F. J. Harris. "On the use of windows for harmonic analysis with the discrete Fourier transform".
In: *Proceedings of the IEEE* 66.1 (1978), pp. 51–83 (cit. on p. 25).

[51] J. A. Nelder and R. Mead. "A Simplex Method for Function Minimization".
In: *The Computer Journal* 7.4 (Jan. 1965), pp. 308–313. ISSN: 0010-4620.
DOI: 10.1093/comjnl/7.4.308. eprint:
https://academic.oup.com/comjnl/article-pdf/7/4/308/1013182/7-4-308.pdf.
URL: https://doi.org/10.1093/comjnl/7.4.308 (cit. on p. 26).

[52] W. H. Press et al. *Numerical Recipes 3rd Edition: The Art of Scientific Computing*. 3rd ed.
USA: Cambridge University Press, 2007. ISBN: 0521880688 (cit. on p. 27).

[53] A. D. Boozer et al. "Cooling to the Ground State of Axial Motion for One Atom Strongly Coupled to an Optical Cavity". In: *Phys. Rev. Lett.* 97 (8 Aug. 2006), p. 083602.
DOI: 10.1103/PhysRevLett.97.083602.
URL: https://link.aps.org/doi/10.1103/PhysRevLett.97.083602 (cit. on p. 35).

[54] M. H. Anderson et al. "Observation of Bose-Einstein Condensation in a Dilute Atomic Vapor".
In: *Science* 269.5221 (1995), pp. 198–201. ISSN: 0036-8075.
DOI: 10.1126/science.269.5221.198.
eprint: https://science.sciencemag.org/content/269/5221/198.full.pdf.
URL: https://science.sciencemag.org/content/269/5221/198 (cit. on p. 35).

[55] A. D. Boozer. "Theory of Raman transitions in cavity QED".
In: *Phys. Rev. A* 78 (3 Sept. 2008), p. 033406. DOI: 10.1103/PhysRevA.78.033406.
URL: https://link.aps.org/doi/10.1103/PhysRevA.78.033406 (cit. on p. 35).

[56] M. Ammenwerth. *Analysing a phase-frequency lock of a laser to an optical frequency comb*.
Bachelor's Thesis. 2017 (cit. on p. 37).

[57] L. Ahlheit.
Frequenzvariable Phasenstabilisierung eines Diodenlasers auf einen optischen Frequenzkamm.
Bachelor's Thesis. 2017 (cit. on p. 37).

[58] E. D. Black. "An introduction to Pound–Drever–Hall laser frequency stabilization".
In: *American Journal of Physics* 69.1 (2001), pp. 79–87. DOI: 10.1119/1.1286663.
eprint: https://doi.org/10.1119/1.1286663.
URL: https://doi.org/10.1119/1.1286663 (cit. on p. 39).

[59] D. Leibfried et al. "Quantum dynamics of single trapped ions".
In: *Rev. Mod. Phys.* 75 (1 Mar. 2003), pp. 281–324. DOI: 10.1103/RevModPhys.75.281.
URL: https://link.aps.org/doi/10.1103/RevModPhys.75.281 (cit. on p. 40).

[60] W. Alt. "Optical control of single neutral atoms". PhD thesis. 2004 (cit. on p. 41).

[61] V. Makhalov et al. “Precision measurement of a trapping potential for an ultracold gas”.
In: *Physics Letters A* 379.4 (2015), pp. 327–332. ISSN: 0375-9601.
DOI: https://doi.org/10.1016/j.physleta.2014.10.049.
URL: http://www.sciencedirect.com/science/article/pii/S0375960114012055
(cit. on pp. 43, 47).

[62] T. A. Savard, K. M. O’Hara and J. E. Thomas.
“Laser Noise Induced Heating in Far Off Resonance Optical Traps”.
In: *Quantum Electronics and Laser Science Conference*. Optical Society of America, 1997, QPD6.
URL: http://www.osapublishing.org/abstract.cfm?URI=QELS-1997-QPD6
(cit. on pp. 43, 47).

[63] B. J. Lester, A. M. Kaufman and C. A. Regal.
“Raman cooling imaging: Detecting single atoms near their ground state of motion”.
In: *Phys. Rev. A* 90 (1 July 2014), p. 011804. DOI: 10.1103/PhysRevA.90.011804.
URL: https://link.aps.org/doi/10.1103/PhysRevA.90.011804 (cit. on pp. 45, 47).